Temporal variations of Venusian upper cloud and haze inferred from ground-based polarimetric observations

ENOMOTO TAKAYUKI

Doctor of Philosophy

Department of Space and Astronautical Science
School of Physical Sciences
SOKENDAI (The Graduate University for Advanced Studies)

Temporal variations of Venusian upper cloud and haze inferred from ground-based polarimetric observations

[地上からの偏光観測による金星上層の雲・ヘイズの時間変化に関する研究]

Takayuki Enomoto

January 10, 2017

Abstract

Venus is entirely shrouded by thick clouds composed of micron-sized droplets of concentrated sulfuric acid (H_2SO_4). In addition to the main cloud, it is known that the submicron hazes overlay and vary with time scale of several years. These particles play important roles in the upper atmosphere of Venus by scattering and absorbing the incident sunlight, thereby affecting the temperature and the chemistry. Therefore, studying generation and sustention mechanism of the massive cloud system is essential for deep understanding of the chemical process, radiative balance of the atmosphere, and atmospheric dynamics. With such background, this thesis focuses on spatial and temporal variability of clouds and hazes of Venus. Three major achievements of this thesis are: A) large-scale temporal variations of the haze are detected and characterized by ground-based observations; B) physical parameters are derived by comparing the observations with model simulations; and C) a possible factor for the temporal variations of haze is proposed.

A) Tracking the temporal variations of the haze

To efficiently study variability of submicron hazes, appropriate observing wavelengths (930 nm for haze abundances and 438 nm for cloud-top altitudes) and solar phase angles (∼80 degrees) are chosen. Then, strategic imaging-polarimetric observations were carried out from August 2012 to June

2015 with HOPS (Hida Optical Polarimetry System) instrument attached to the 65-cm refractor telescope at the Hida Observatory. In addition to the standard processing of polarimetry data, I have developed a procedure to reduce the effect of atmospheric seeing: both disk-integrated polarizations and spatially-resolved polarization maps are produced from raw HOPS data. I measure the disk-integrated polarizations with a technique of aperture photometry, which minimizes the blurring effect due to the atmospheric seeing. Then, I estimate a point-spread function (PSF: a modified-Lorentzian function is introduced) for each image, by blurring a synthetic image to match the observed image, which is used in the model comparisons. In the time series (August 2012, April 2014, and June 2015), a significant change in the disk-integrated polarizations (from -2.2% to -3.6%) is detected. The polarization maps also show large changes in spatial distribution of the haze. The positive polarizations seen in polar regions in August 2012, turned to be negative in April 2014 and June 2015. Such a large-scale variability is reported for the first time since the end of the Pioneer Venus mission.

B) Derivation of physical parameters for the haze variations

To estimate the properties of the haze, I compared observations with theoretical calculations. For model calculations, I refer to Sato et al. (1996) as the vertical structure model, which approximate well the structure of upper cloud of Venus. Optimal parameter space is searched for by comparing the disk-integrated polarizations and the polarization maps with the model computations after blurring with the measured PSF. From the comparisons of 930nm data, I found optical thickness of upper haze τ_h=0.15 and fraction of the haze in cloud layer f_h=0.047 in August 2012, decreasing to τ_h=0.02 and f_h=0.016 in April 2014, and τ_h=0.01 and f_h=0.01 in June 2015. On

the other hand, from 438nm data, the cloud top altitudes are lower in polar region in August 2012 and June 2015, while these are flat for the entire planet in April 2014. With these results, I have tested the " Cloud lowering hypothesis (Braak et al. (2002)); the haze particles are distributed uniformly in certain altitude over the whole altitude, thus the lowering of the cloud top leaves relatively more of sub-micron particles above the cloud. My finding that τ_h is small while the cloud top altitude on polar region is lower in June 2015 obviously conflicts with that hypothesis. For the first time, such discrepancy is observationally and quantitatively indicated.

C) Possible factor of the temporal variation of haze

In order to explain mechanisms of the variations of haze, I simulated the behavior of τ_h and f_h by altering the cloud top and aerosol scale height profiles by referring to previous studies based on Venus Express [Wilquet et al. (2012), Lee et al. (2012)]. When aerosol scale height is varied, τ_h does not change over some aerosol scale height and f_h increase linearly. From these 2 examinations, I found that the variations of both cloud top altitude and aerosol scale height also cannot explain my observations. However, the simultaneous decrease of f_h and τ_h are realized when the amount of the haze particles is lowered. This shows that the amount of haze itself is the cause of the variation of τ_h and f_h. I propose the relationships to the solar activity as a possible explanation for such variation of haze. To investigate this, I developed a conversion equation from derived τ_h to SO_2 abundance f_{SO_2} of which time history can be found in literature. Esposito et al. (1988) pointed out the correlations in temporal variation of τ_h and f_{SO_2} during PVO mission, which indicate that the source of the haze is SO_2. Using my results and the relationships between them, I estimated the temporal variations of f_{SO_2}. The

values obtained from the relations are consistent with the temporal variation of f_{SO_2} reported by Marcq et al. (2013), if the decrease of f_{SO_2} from 2007 has been continued. I found that several phenomena, such as increases of haze and SO_2, seem to correspond to the solar maxima. The photochemical reactions, thus production of SO_2, might become active since the UV flux increase in solar maximum. In order to confirm the relations between solar activity and SO_2 or τ_h, long-term observations over several ten years are needed for the future.

My observations captured the situation of epic decrease of the haze since 1980 's Pioneer Venus mission by ground-based observations for the first time, which provide new information about the temporal variations of upper haze to the history of Venus. The cause of the temporal variations of the haze and proposed factor to them in this thesis should contribute to the science of Venus in understanding the mechanism of generation and sustention mechanism of the upper haze.

Contents

List of Tables

List of Figures

Chapter 1

Introduction

Venus is entirely shrouded by thick cloud of concentrated sulfuric acid (H_2SO_4). Such particles play important roles in the upper atmosphere of Venus by scattering and absorbing the incident sunlight, thereby affecting the temperature and the chemistry. Therefore, studying generation and sustention mechanism of the massive cloud system is essential for deep understanding of the chemical process, radiative balance of the atmosphere, and atmospheric dynamics.

1.1 Structure of the Venusian cloud

The aerosol particles in the cloud can be characterized into 3 modes in terms of the size; Mode 1 particles with radius $r \sim 0.2\mu$m, mode 2 particles $r \sim 1$ μm, and Mode 3 particles $r \sim 3\mu$m. The cloud is located in altitude from 50 to 70 km. These facts are clarified from several *in situ* measurements by entry probes [cf. Knollenberg and Hunten (1980)]. This cloud layer can be categorized to cloud layers (Upper, Middle, and Lower cloud layer) and 2 haze layers (Upper, and Lower haze layer) as listed in table 1.1 [Esposito et al.

(1983)]. Since half of the absorption of incident sunlight in the atmosphere occurs at altitude around 60km [Tomasko et al. (1980)], the existence of the cloud is important in terms of energy deposition.

Table 1.1: Vertical structure of Venusian cloud [Esposito et al. (1983)]. Numbers in parenthesis are modes of particles.

Region	Altitude (km)	Temperature (K)	Optical Depth τ at 630nm	Average Number Density (N cm^{-3})	Mean Diameter (μm)	Proposed Composition
Upper haze	70-90	225-190	0.2-1.0	500	0.4	H_2SO_4+ contaminants
Upper cloud	56.5-70	286-225	6.0-8.0	1500(1) 50(2)	Bimodal 0.4&2.0	H_2SO_4+ contaminants
Middle cloud	50.5-56.5	345-286	8.0-10.0	300(1) 50(2) 10(3)	Trimodal 0.3, 2.5, & 7.0	H_2SO_4+ crystal(?)
Lower cloud	47.5-50.0	367-345	6.0-12.0	1200(1) 50(2) 50(3)	Trimodal 0.4, 2.0, & 8.0	H_2SO_4+ crystal(?)
Lower haze	31-47.5	482-367	0.1-0.2	2-20	0.2	H_2SO_4+ contaminants
Precloud layers	46 & 47.5	378 & 367	0.05 & 0.1	50 & 150	Bimodal 0.3 & 2.0	H_2SO_4+ contaminants

The latitudinal dependence of the cloud top have been studied by several authors . Lee et al. (2012) studied about the latitudinal dependence of the cloud top altitude in terms of remote sensing by analyzing near-infrared spectroscopic data by VIRTIS (Visible and Infrared Thermal Imaging Spectrometer) and temperature profile by VeRa (Venus Radio Science: Radio sounding experiment), both onboard Venus Express, and showed the latitudinal profile of the cloud top altitude and aerosol scale height (Figure 1.1). The cloud top altitude from equatorial to middle latitude ($\sim$50°) is around

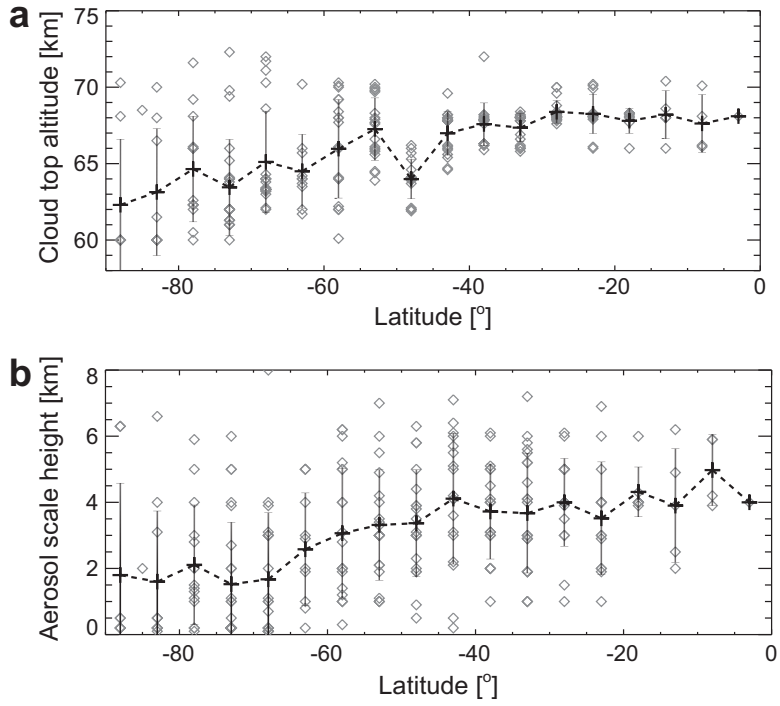

Figure 1.1: a: Cloud top altitude along latitude. b: Aerosol scale height along latitude. (Lee et al. (2012))

68km level, but decreases with latitude to 62km level. Although the cloud top altitudes are different for wavelength, such variations were observed in

other wavelength regions (cf. Zasova et al. (2007), Ignatiev et al. (2009)). The similar variation was observed for aerosol scale height, which shows similar decrease with latitude, from ∼4km in equatorial to middle latitude region to 2km in polar region.

These variations in vertical and horizontal structure of the cloud are important in terms of energy balance, because these variations can change the profiles of the atmospheric heating. At the same time, they are also important for remote sensing since these variation can affect the morphology, thus interpretation of the observations.

1.2 Model of chemistry of the cloud and its advection

The source of the cloud is thought to be SO_2 in the atmosphere. SO_2 is oxidized by photochemically-produced O atoms,

$$SO_2 + O + M \rightarrow SO_3 + M, \tag{1.1}$$

and SO_3 reacts with H_2O, and is transformed to H_2SO_4,

$$SO_3 + H_2O \rightarrow H_2SO_4. \tag{1.2}$$

These reactions, thus the production of cloud particles, mainly occur at ∼62 km altitude within a thin layer of few kilometers [Yung and Demore (1982), Krasnopolskii and Parshev (1983)]. While there is few observational proof about meridional circulation in Venusian atmosphere, we show here a model that includes advection of chemical materials proposed by Imamura and Hashimoto (1998). Generated cloud particles are transported by poleward advection, which is confirmed by cloud tracking study by Rossow et al.

(1990) and is regarded as upper part of the meridional circulation, to polar regions. Around the poles, sedimentation occurs and cloud particles evaporate below the cloud bottom.

]

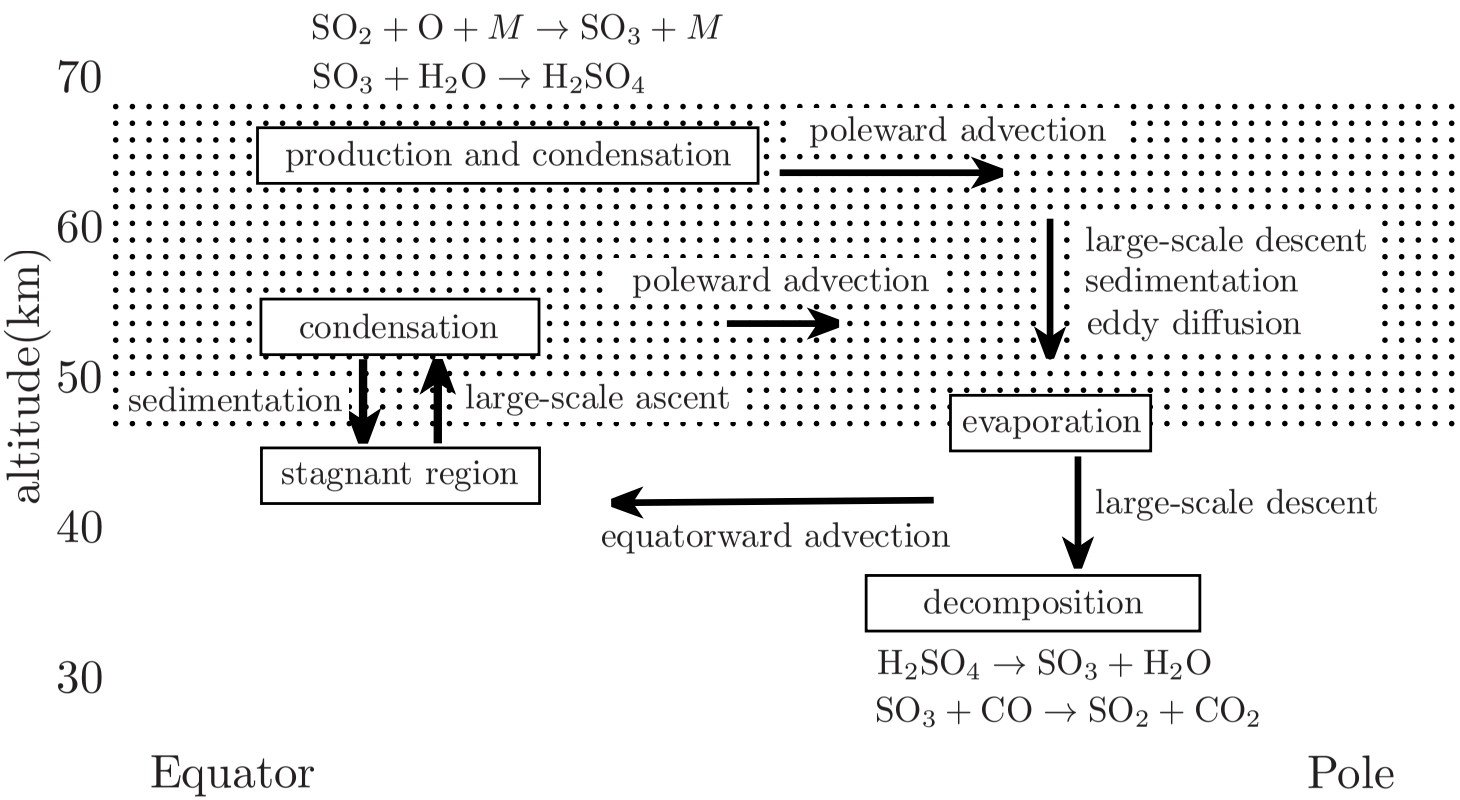

Figure 1.2: Schematic view of atmospheric circulation

1.3 Polarimetry of Venus

Polarimetry is a powerful tool to investigate cloud particle size and refractive index, and cloud vertical structure. The first systematic polarimetric analysis was carried out by Hansen and Hovenier (1974), who analyzed 1950's and 1960's ground-based data of disk-averaged polarization (Figure 1.3). The]

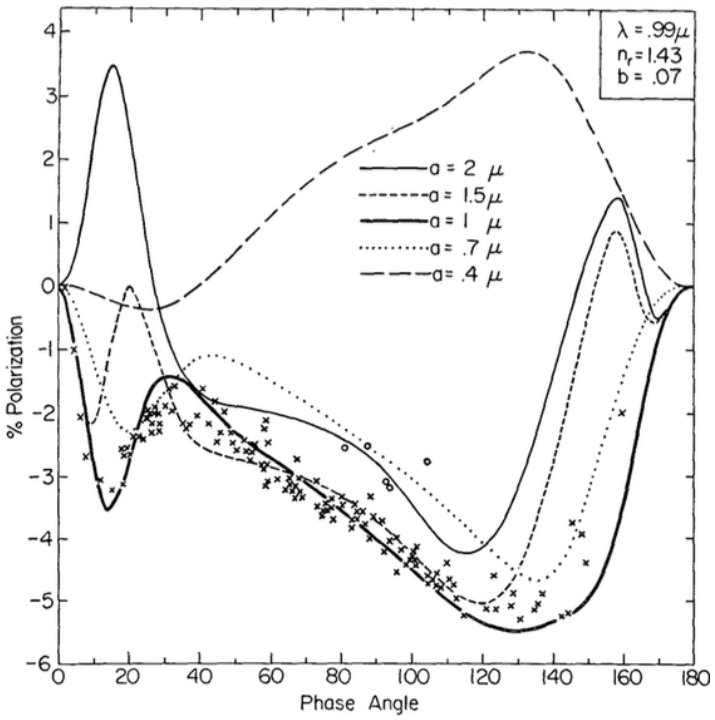

Figure 1.3: A comparison between theoretical models (lines) for several effective radius a of cloud particles and observations (points) at $\lambda = 990$nm obtained in 1950's and 1960's. Since the curves strongly respond to the variations of the parameters, parameters of cloud particles can be accurately estimated.

cloud model used in the radiative transfer calculations was simple semi-

infinite cloud composed of micron-sized cloud particles. The refractive index of the cloud particle was $n_r = 1.43$ at λ=990nm, and the effective radius and variance in a particle size distribution were $r_{\rm eff}$=1.05μm and $v_{\rm eff}$=0.07, respectively. The wavelength dependence of the refractive index indicated 75% H_2SO_4 solution as composition of cloud particles. Kawabata et al. (1980) analyzed polarimetric data taken by Orbiter Cloud Photo-polarimeter (OCPP) onboard Pioneer Venus Orbiter (PVO) in early period of the mission. They found that there was a large amount of submicron-sized particles, "hazes", distributed mixed in and above the cloud layer. The properties of these particles are $r_{\rm eff}$=0.23μm, $v_{\rm eff}$=0.18 and $n_r = 1.45$ at λ =935nm, which has no conflicts with sulfuric acid. Additionally, the spatial distribution of the upper haze was not uniform. While the optical thickness of upper haze on the equatorial region was 0.02, that on both polar regions was 0.3 at λ=935nm. Temporal variations of such parameters were also reported by several authors (e.g. Sato et al. (1996), Knibbe et al. (1998), Braak et al. (2002)). Sato et al. (1996) reported that the optical thickness of upper hazes on Northern polar region decreased from 0.3 to 0.05 at λ=935nm during the first 2820 days of PVO mission period, and the properties of hazes ($r_{\rm eff}$=0.25μm, $v_{\rm eff}$=0.17 and $n_r = 1.43$ at λ =935nm) were quite stable in its mission period. Recently, European Venus exploration spacecraft, Venus Express (VEx), investigated physical and chemical properties of aerosols in the upper atmosphere from various aspects. As a recent polarimetric study, the preliminary results of Rossi et al. (2015) with polarimetric observations from SPICAV instrument showed that though there were time variations in the optical thickness of the upper hazes, the upper limit of them in 2010 is 0.17 at $\lambda = 1.101\mu$m, which is comparable with the value of Kawabata et al. (1980).

The temporal variation is pointed out to be related to the amount of

SO_2 in the atmosphere since they have positive correlation in long-term variation (Esposito et al. (1988)). However, there is no study about the correlations after PVO mission while Marcq et al. (2013) reported that the amount of SO_2 had decreased in the mission period of Venus Express from 2007.

1.4 The objectives of this study

In order to achieve the knowledge of generation and sustention mechanism of Venusian upper haze, we set goals of this study as (1) Track the temporal variations of the haze by carrying out ground-based observations, (2) Interpret the obtained physical parameters by simulations with known physical properties, and (3) Propose the possible factor for the temporal variations of haze.

Chapter 2

Methodology

2.1 Observation

2.1.1 Imaging-polarimeter "HOPS" and Hida 65-cm refractor telescope

Polarimetric observations were performed with an imaging-polarimeter "HOPS" (an acronym of Hida Optical Polarimetry System) attached to the 65-cm refracting telescope (figure 2.1) at the Hida Observatory of the Kyoto University (Takayama, Gifu, Japan). This telescope (the focal length is 10.5 m) is favored for polarimetry of planets for 3 reasons: 1) the atmospheric condition is relatively stable at the site; 2) the telescope's long optical tube is supported by a robust structure; and 3) the optics is perfectly symmetry with no reflecting mirror or obstacle throughout the ray path.

A set of chromatic-aberration correction lenses is inserted between the 65-cm objective lens and HOPS. There are 3 positions: lens B is for short wavelengths (400–500 nm); lens R is for 600 nm and longer wavelengths; and blank for wavelengths between 500 and 600 nm.

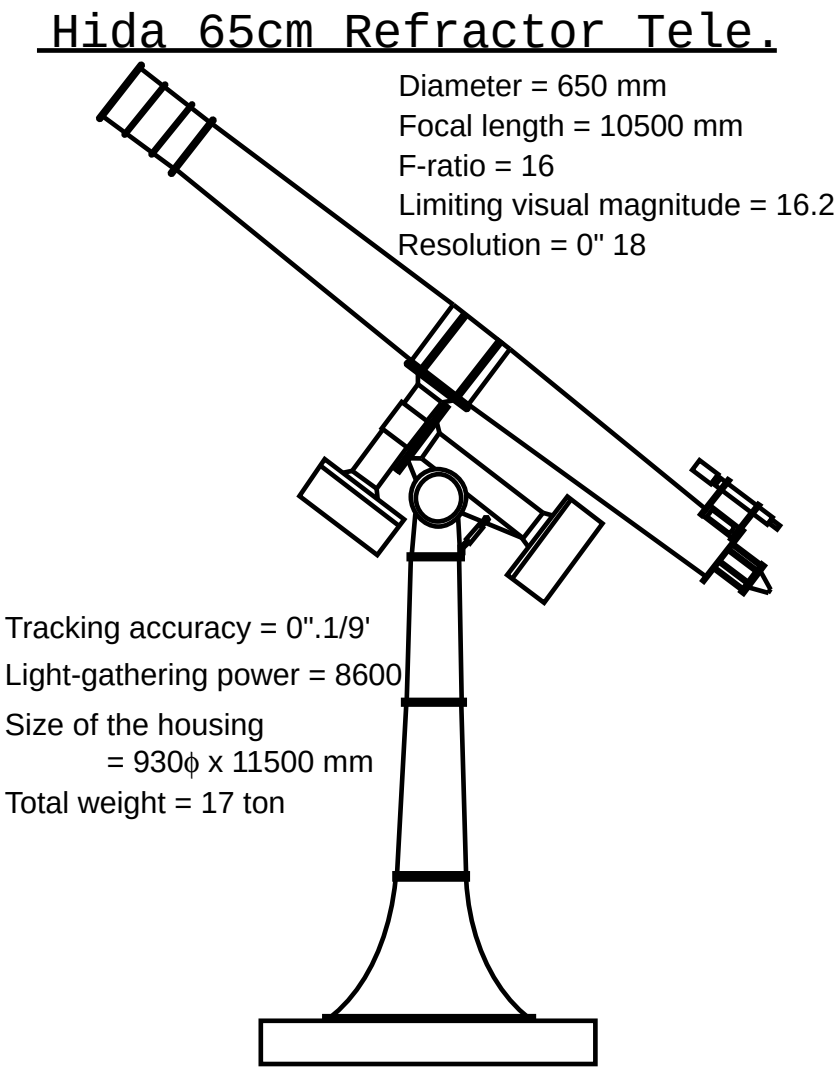

Figure 2.1: An illustration of the Hida 65-cm refractor telescope from Web site of the Hida observatory (https://www.kwasan.kyoto-u.ac.jp/general/facilities/65cm/).

HOPS is a 2-beam type imaging polarimetry instrument (Satoh et al. (2001)), which consists of a super-achromatic half-wave retarder plate (on a rotating mount) and a single Wollaston prism. The optical system of the instrument is shown in figure 2.2.

Table 2.1: Properties of CCD

Pixel format	1024 pixel × 1024 pixel
Length of the side of a pixel	24μm
Length of the side of the CCD detector	24.6 mm × 24.6 mm

Table 2.2: Properties of filters. FWHM is full width at half maximum.

Filter name	Central wavelength	FWHM	Integration time	Plate scale
IR	930nm	10nm	6 s	0.329 ″/pixel
Red	650nm	10nm	0.15 s	0.323 ″/pixel
Green	546nm	10nm	0.12 s	0.288 ″/pixel
Blue	438nm	10nm	0.12 s	0.328 ″/pixel

The detector is a Peltier-cooled CCD (SBIG, STL-1001E), of which properties are listed in table 2.1. HOPS has a set of 4 narrow-band filters, λ=438nm (Blue), 546nm (Green), 650nm (Red), and 930nm (IR). The properties are listed in table 2.2.

2.1.2 Description of polarization state

State of polarization of observed light can be described by a set of Stokes parameters, I, Q, and U. Another Stokes parameter, V, which describes circular polarization, is not considered here as reflected sunlight from Venus is known to have very little circular polarization (Kawata (1978)). Two parameters, Q, and U, are interchangeable as the coordinate system is rotated, and U becomes almost zero when the intensity equatorial plane (a plane which

includes the sun, center of Venus, and the observer) is taken as a reference plane from which position angle of (Q, U) vector is measured. Therefore, we hereafter call Q/I "degree of linear polarization" (DOLP). In this case, positive Q corresponds to the polarization with the vibration perpendicular to the reference plane.

2.1.3 Phase angle and observing wavelength

To extract physical information of the haze layer from the data most efficiently, we have carried out observations and chosen the data that satisfy following two conditions: the phase angle α is $\sim 80°$, and the data were taken with the IR filter. The reasons are:

1. Contrast of polarizations between haze and cloud is maximum in IR,
2. apparent diameter of Venus is sufficient to overcome the seeing effect, and
3. elongation to the sun is large, thus stray light from the sun is minimized.

Since observed DOLPs are the results of multiple light scattering in the atmosphere, they should be smaller than those of single scattering. But the characteristics, such as the sign of DOLP and the phase angle α making DOLP 0%, is not significantly different from that of single scattering, so we can estimate the combinations of α and λ most sensitive to the amount of hazes, based on theoretical calculations of single scattering polarizations. Figure 2.3 shows the phase angle and wavelength dependence of p_h and p_c, theoretical DOLP of single scattering generated by haze and cloud particles, and polarization contrast (PC) defined as $PC = p_h - p_c$.

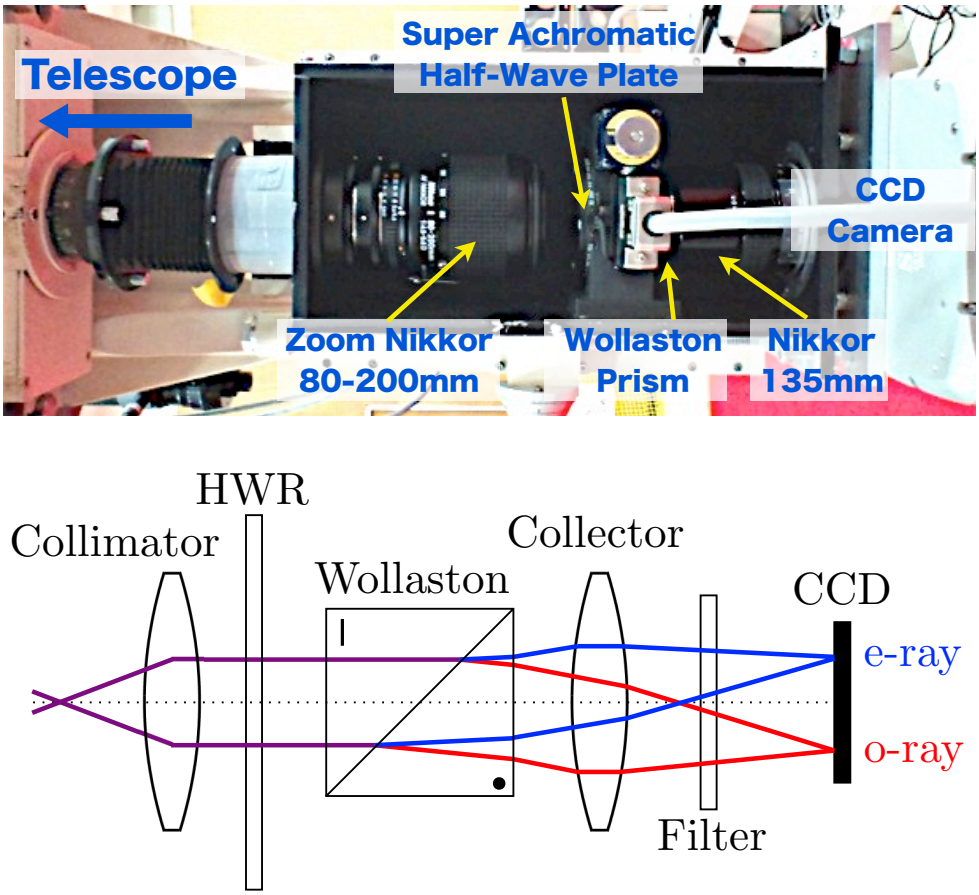

Figure 2.2: Upper picture is the exterior view, and lower figure is the schematics of the optical system of HOPS. The collected light from the telescope is collimated through Zoom Nikkor (Collimator). The collimated light passes through the half-wave retarder (HWR) and Wollaston prism, and again collected on the surface of the CCD detector by Nikkor (Collector). The symbols "|" and "•" indicate the direction of the optic axis of the calcite, parallel and perpendicular to the plane of paper, respectively. At the same time, the directions of vibration of e-ray and o-ray is perpendicular and parallel to the plane of paper. The optical system is obscured by blackout curtain to avoid stray light from outside.

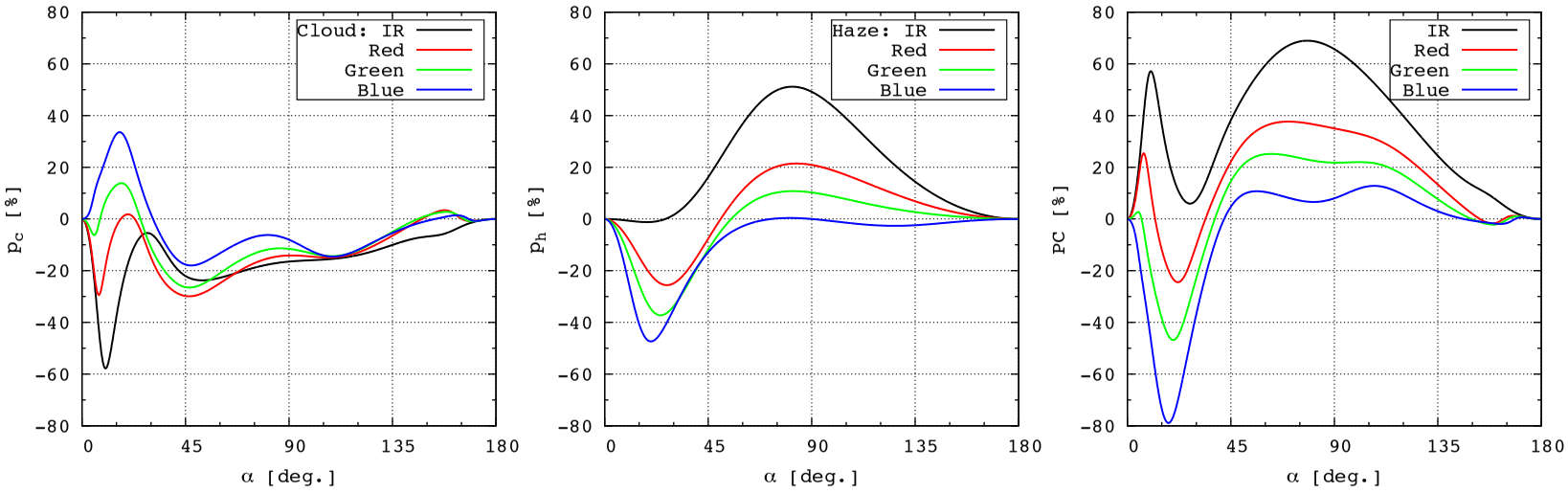

Figure 2.3: Single scattering DOPL from cloud and haze particles (left and center), and polarization contrast between them (right). Polarization contrast (PC) is the difference of the single scattering degree of polarization between haze and cloud particles. These DOLPs are calculated for r_{eff}=1.05μm, v_{eff}=0.07, n_r =1.43 (for IR), 1.45 (for Red, Green, Blue). The larger the PC is, the more sensitive polarimetric observations get.

The sensitivity to the amount of haze is higher for large positive or negative PC; (1) $\alpha \sim 20°$, λ=438nm and (2) $\alpha \sim 80°$, λ=930nm. Because the apparent diameter of Venus at $\alpha \sim 20°$ is smaller than $16''$ as mentioned in the above, the polarization map at $\sim 20°$ phase angle will not be used while $\alpha \sim 80°$ may be used if the seeing was good. In addition, the data at small or large α (near 0° or 180°) may be affected by sunlight as elongation to the sun is small. We therefore selected the data satisfying the condition (2) as the most useful combination of phase angle and observing wavelength. Details of observational condition are listed in the Result section. Additionally, cloud top altitude can be estimated from Blue data by considering Rayleigh scattering. The polarization degrees of single scattering by Rayleigh scattering can be described as

$$p(\alpha) = \frac{\sin^2 \alpha}{1 + \cos^2 \alpha + 2\rho_n/(1 - \rho_n)}, \tag{2.1}$$

where α is phase angle and ρ_n is the depolarization factor, which depends on the kind of molecule (The shape of this function is shown in figure 2.4). This function gets maximum at $\alpha = 90°$ and p_c is close to 0% in this wavelength at this phase angle, it is convenient to perform this analysis with this condition.

2.2 Data reduction

2.2.1 Dark current and flat field correction

Although linearity of CCD device is superb, it requires two major corrections. One is the dark noise, which is caused by thermally-generated electrons in Si substrate. A Peltier cooler keeps the CCD at a stable low temperature, reducing the noise and maintaining it at a constant level (electrons per pixel per second). Another is non-uniformity of sensitivity. Since this non-uniformity

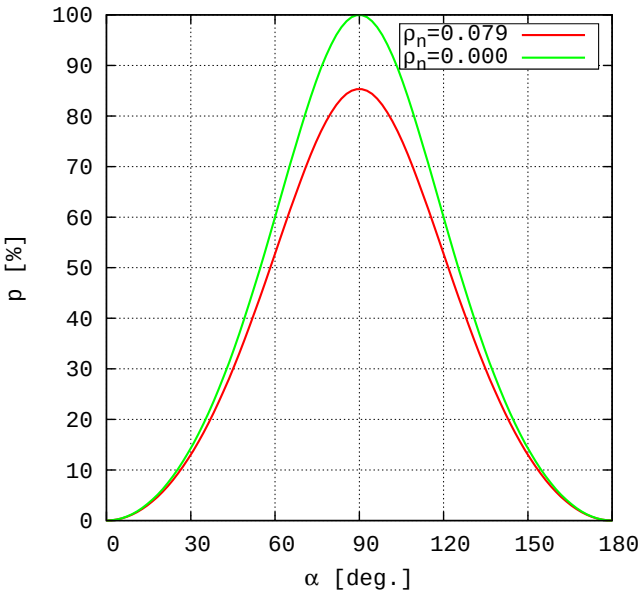

Figure 2.4: Phase angle dependence of single scattering polarization p of Rayleigh scattering. α is phase angle. $\rho_n = 0.079$ corresponds to CO_2 molecules, and $\rho_n = 0$ corresponds to the isotropic molecules.

is permanent feature and is fixed to pixels, this can be removed by dividing an object image by a flat-field image. A flat-field can be obtained by imaging a uniformly-illuminated object. In this study, we took clear sky by pointing the telescope to the zenith.

Because a flat-field image F also includes dark current D, one raw image R can be processed to obtain a corrected image C as follows:

$$C = \frac{(R - D)}{(F - D)/N}, \tag{2.2}$$

where N is a normalization factor of $F - D$ image.

2.2.2 Derivation of Degree of Linear Polarization (DOLP)

A 2-beam type polarimeter measures intensities of light in 2 beams (called ordinary and extraordinary rays) oscillating in planes perpendicular to each other. By repeating measurements for 4 position angles ($0°, 22.5°, 45°$, and $67.5°$) of a half-wave retarder plate, this type of instrument allows polarimetry of high accuracy (Tinbergen (1996)). The degrees of linear polarization are calculated by following equations (Tinbergen (1996));

$$\frac{Q}{I} = \frac{1-a_1}{1+a_1} \tag{2.3}$$

$$\text{with } a_1 = \sqrt{\frac{I_e(0°)}{I_o(0°)} \Big/ \frac{I_e(45°)}{I_o(45°)}}$$

$$\frac{U}{I} = \frac{1-a_2}{1+a_2} \tag{2.4}$$

$$\text{with } a_2 = \sqrt{\frac{I_e(22.5°)}{I_o(22.5°)} \Big/ \frac{I_e(67.5°)}{I_o(67.5°)}}$$

where $I_o(\phi)$ and $I_e(\phi)$ are intensities of the light separated for ordinary and extraordinary ray, respectively; ϕ is the position angle of half-wave plate installed in front of a Wollaston prism.

2.2.3 Calibration of instrumental polarizations

Although the optics of HOPS and the 65-cm telescope is symmetry, there still remain instrumental polarizations of small amplitudes. We have carefully examined flat-field images (acquired in the daytime of observing run) and obtained experimental values of such polarization as a function of position in the field of view. In the data analysis, the Venus data are corrected for by subtracting the instrumental polarization.

2.2.4 Consideration of atmospheric seeing

One major and unavoidable problem of ground-based observation is variable atmospheric seeing, which blurs the image and alters the intensity distribution over the planetary disk with different degrees from one image to another. This obviously could cause errors in polarimetry as the seeing changes while we acquire a set of images at 4 position angles of the half-wave retarder plate in HOPS. In order to reduce the effect of atmospheric seeing, we perform both aperture photometry and analysis of 2-dimensional polarization maps. The aperture photometry is a way to avoid the effect of atmospheric seeing, in sacrifice of spatial information, by measuring polarization of integrated light from the object. On the other hand, to better utilize information of 2-dimensional polarization maps from HOPS, the data are filtered by the "measured" seeing size. If the seeing size is larger than 14 in γ described in equation (2.20), corresponding 2-dimensional map is discarded.

Figure 2.5 illustrates an example of aperture photometry of Venus. An aperture is a circular region of which radius $R_{\rm ap}$ is large enough to integrate super-majority of light from the object. An annulus, used to determine the background level, is a region between two circles with radius $R_{\rm an}$ and $R_{\rm an} + \Delta R_{\rm an}$ large enough to avoid the tail of blurred light of the object.

Intensities of the object $I_{\rm obj}$, Venus in this study, are calculated by the following equation;

$$I_{\rm obj} = \sum_{i=1}^{N_{\rm ap}} I_i - N_{\rm ap} I_{\rm bg} \tag{2.5}$$

$$I_{\rm bg} = \sum_{j=1}^{N_{\rm an}} I_j / N_{\rm an} \tag{2.6}$$

where $N_{\rm ap}$ and $N_{\rm an}$ are the number of pixels in the aperture and the annulus, respectively.

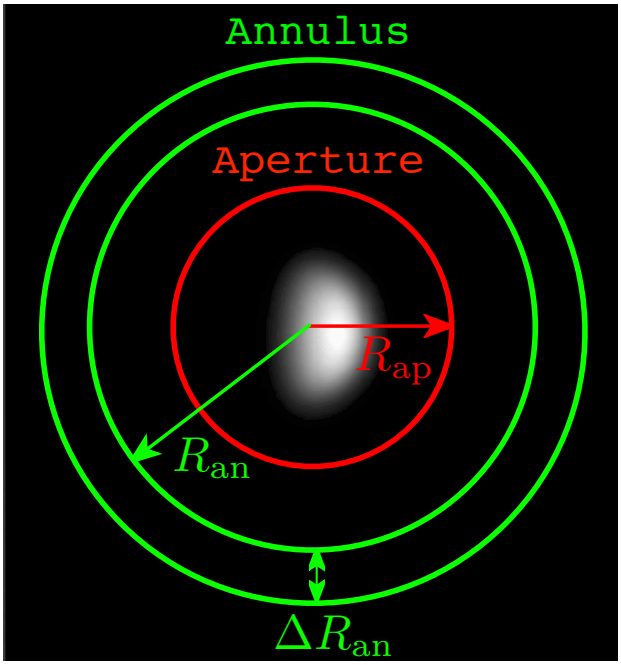

Figure 2.5: An example of aperture photometry. An aperture region surrounded by a red circle with radius $R_{\rm ap}$ is for measuring the intensity of the object including back ground sky counts. The annulus region enclosed between two green circles with radius $R_{\rm ap}$ and $R_{\rm ap} + \Delta R_{\rm ap}$ is for measuring back ground sky counts.

In order to determine the size of aperture and annulus, we performed test calculations for several combinations of these parameters. Figure 2.6 shows an example of the aperture and annulus dependence of DOLP for April 2014 set01 data with angular radius of Venus $R_{\rm v} = 27.5$ pixels. The data points are DOLP for $R_{\rm ap} = 30$, 40, and 50 pixels, and $R_{\rm ap}$ from corresponding value of $R_{\rm ap}$. $\Delta R_{\rm ap}$ is fixed to 5 pixels. In case of $R_{\rm ap} = 30$ pixels, the DOLP is negatively overestimated because the aperture is slightly small to integrate all the light from the object blurred by the atmospheric seeing. On the

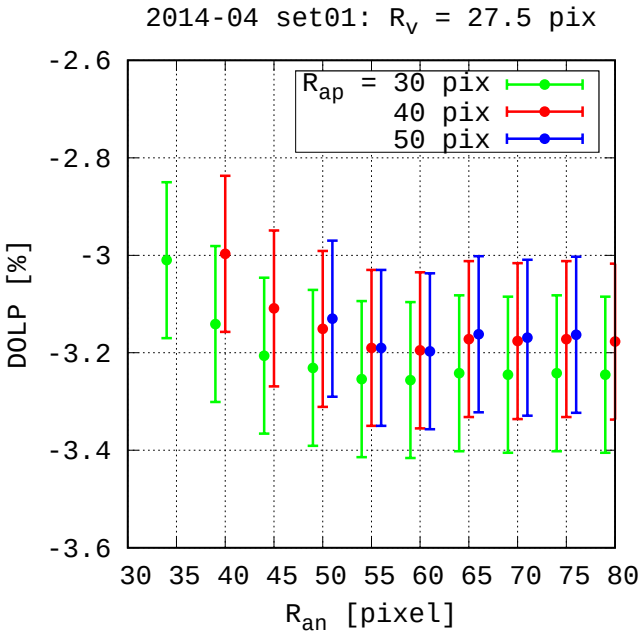

Figure 2.6: Aperture and annulus dependence of the polarization degrees. Points for $R_{\rm an}$ = 30 and 50 pixels are shifted by ± 1 pixels for easiness to distinguish different aperture each other.

other hand, DOLP with $R_{\rm ap}$=40, and 50 pixels for over $R_{\rm an}$ = 55 pixels is stable, which means that the tail of the blurred light converges around $R_{\rm ap}$ = 40pixels. Since enlarging the value of $R_{\rm ap}$ too much may carry a risk of involving unexpected errors, we determined the size of aperture and annulus as $R_{\rm ap} = 1.5R_{\rm v}$, and $R_{\rm an} = R_{\rm ap} + 15$ pixels, respectively.

2.3 Model calculation

Numerical computation of the polarized light from Venus is done in 3 steps:

1. A single scattering matrix (a transformation matrix between Stokes

parameters of the incident light and the scattered light) based on Mie theory is obtained with a published computational code by Mishchenko et al. (2002).

2. Using the resultant single scattering matrix, we carry out radiative transfer calculations with the effect of multiple light scattering is taken into account for. Computational code for this has been domestically developed by referring to de Haan et al. (1987) and Hovenier et al. (2004).

3. A model polarization map is produced by pixel-by-pixel computations of I and Q for scattering geometries of individual pixels. Obtained map is then blurred with an appropriate point-spread function (PSF) discussed in the followings.

2.3.1 Cloud structure model

We define cloud, haze, and molecular particles as follows;

Cloud $r_{\rm eff}$=1.05μm, $v_{\rm eff}$=0.07, n_r, and $\varpi_{0,c}$

Haze $r_{\rm eff}$=0.25μm, $v_{\rm eff}$=0.17, n_r, and $\varpi_{0,h}$

Molecule CO_2 molecule, with depolarization factor $\rho_n = 0.079$, and $\varpi_{0,m}$

where n_r is real part of the refractive index, and ϖ_0 is the single scattering albedo. n_r is fixed to $n_r = 1.43$ and 1.45 for IR and Blue, respectively. $r_{\rm eff}$, $v_{\rm eff}$, and n_r are taken from previous studies (cf. Sato et al. (1996), Knibbe et al. (1998),Braak et al. (2002)). These values were quite stable through 8 years from the starting date of PVO mission[Sato et al. (1996)]. The size distribution of the particles is a modified gamma distribution function

described as

$$N(r) = Cr^{-3+(1/v_{\rm eff})} \exp\left(-\frac{r}{r_{\rm eff} v_{\rm eff}}\right), \tag{2.7}$$

where C is a constant for normalization. Single scattering albedos of the cloud particles are calculated to force spherical albedo to match that of observed with the similarity relation

$$\varpi_0 = 1 - (1 - \varpi_0^{\rm iso})(1 - \langle \cos\theta \rangle), \tag{2.8}$$

where $\varpi_0^{\rm iso}$ is the single scattering albedo of the isotropic scattering with $\tau = \infty$, and $\langle \cos\theta \rangle$ is the asymmetry parameter of the phase matrix of the assumed particles [Hansen and Hovenier (1974)]. From Chamberlain and Smith (1970) and Mie scattering calculation, we have $\varpi_0^{\rm iso}$=0.99741 and 0.97940, and $\langle \cos\theta \rangle$=0.702 and 0.75 for λ =930nm and 438nm, respectively. Then single scattering albedo of cloud particles are calculated to be $\varpi_{0,c}$ =0.99923 and 0.99485 for λ =930nm and 438nm, respectively. Single scattering albedo of haze and molecules, $\varpi_{0,h}$ and $\varpi_{0,m}$, were fixed to 1 because contributions of the hazes to the spherical albedo are small compared with that of cloud particles, and absorption by CO_2 molecule is small in visible to near infrared (λ <1000nm) range [Moroz (1983)].

Rayleigh scattering from molecules is not included in the analysis at λ =930nm because the contribution from gas molecules is sufficiently small at this wavelength; The scattering cross section of Rayleigh scattering is proportional to λ^{-4} and can produce few contribution to observed polarizations at longer wavelength (the scattering cross section at 930nm is less than 5% of that at 438nm). However, the contribution of the Rayleigh scattering at λ =438nm is significant, Rayleigh scattering is considered in model calculations at this wavelength for estimation of cloud top altitude.

ρ_n is the depolarization factor, which characterizes the polarization degree of Rayleigh scattering. Though the polarization degree from an isotropic

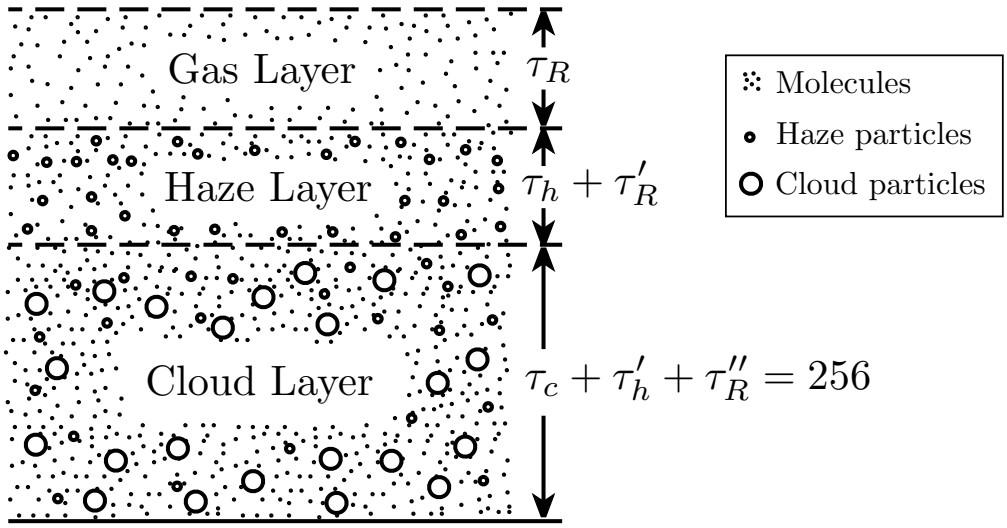

Figure 2.7: Vertical cloud structure model. The vertical cloud structure model is considered after Kawabata et al. (1980). Molecules are neglected in the analysis of IR data.

molecule at phase angle of 90° is 100%, that from an unisotropic molecule is lower than 100%. Therefore, this value depends on the kind of molecule. For example, $\rho_n = 0.020$ for N_2, 0.058 for O_2, 0.028 for dry air, and 0.079 for CO_2. Since the atmosphere of Venus is composed of 96.5% CO_2 [Hovenier et al. (2004)], we used $\rho_n = 0.079$.

Figure 2.7 shows the vertical cloud structure model used in radiative transfer calculations. This model is composed of three layers: main "cloud layer", middle "haze layer", and upper "gas layer". Since the multiple scattering of the lights in the atmosphere reduce the features of the polarizations and make them essentially unpolarized, the feature of linear polarizations are mostly determined by the first several orders of the scattering, down to the layers of the optical thickness unity. So we don't have to model the details of the deep cloud layers which were studied with entry probe measurements.

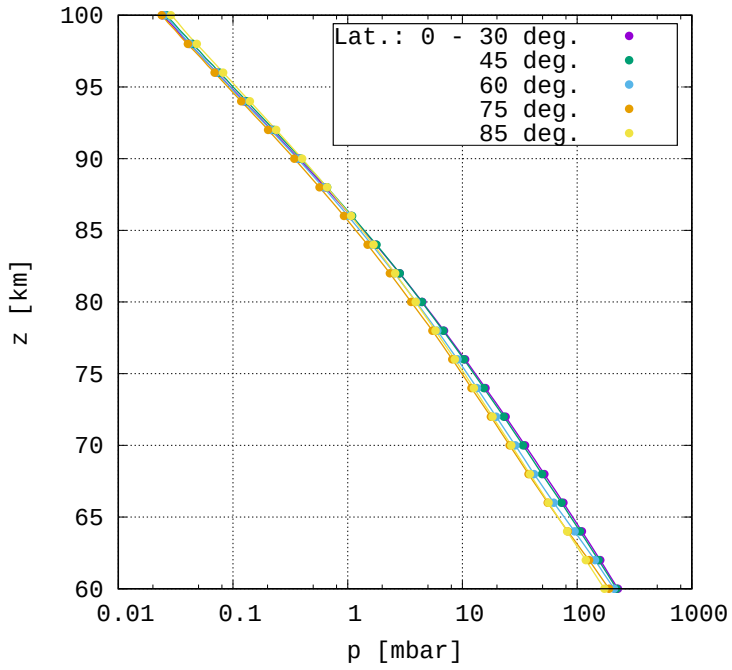

Figure 2.8: The model of the relation between atmospheric pressure and the altitude from the ground. There are 5 models according to the difference of the latitude. In this study, we used $0° - 30°$ data for low to middle latitude region, and $75°$ data for polar regions.

The gas layer is composed only molecules with optical thickness τ_R. τ_R is calculated from the equation

$$\tau_R = \frac{1 + 0.013\lambda^{-2}}{6.17 \times 10^4 \lambda^4} p(z), \tag{2.9}$$

where λ is the wavelength in μm, and $p(z)$ is the pressure in mbar at altitude z (Hansen and Travis (1974)). The relations between pressure p and altitude z are taken form Seiff (1983) as shown in figure 2.8. Calculated optical thickness of gas layer is shown in figure 2.9 for both Blue and IR wavelength. This indicates that the optical thickness of the gas layer for IR wavelength is 5% of Blue wavelength and small enough to neglect at the IR wavelength.

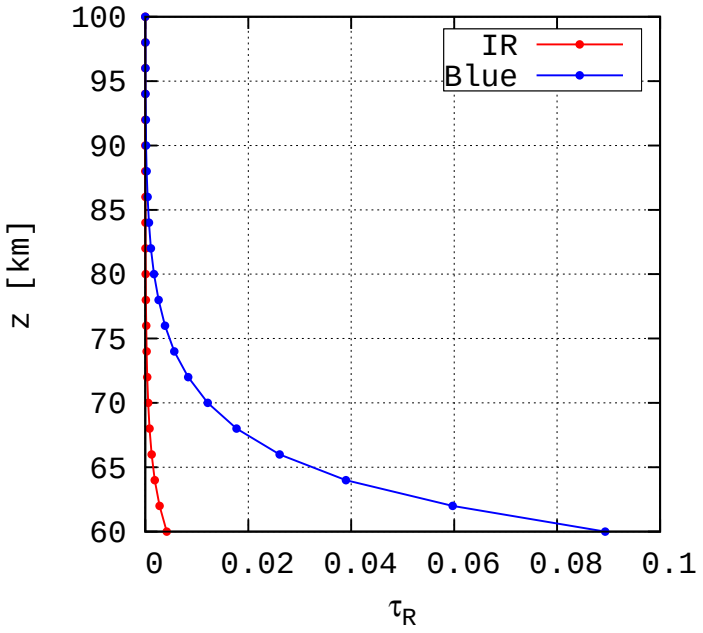

Figure 2.9: Calculated optical thickness. The optical thickness of the gas layer for IR wavelength is about 5% to that for Blue wavelength. Actually this is small enough to be neglected by the altitude of the cloud top around 68km.

The haze layer is composed of haze particles and molecules with optical thickness $\tau_h$and τ'_R, respectively. The main cloud layer is a mixture of cloud, haze particles, and molecules with optical thickness $\tau_c + \tau'_h + \tau''_R = 256$ (virtually semi-infinite). The haze and cloud particles are mixed with the fraction f_h defined by

$$f_h = \frac{k_{\mathrm{sca,h}}}{k_{\mathrm{sca,c}} + k_{\mathrm{sca,h}}}, \tag{2.10}$$

where $k_{\mathrm{sca,h}}$ and $k_{\mathrm{sca,c}}$ are scattering coefficient of haze and cloud particles, respectively. Here we assumed $k_{\mathrm{abs,c}} = 0$ because this factor is smaller by 10^{-5} to $k_{\mathrm{sca,c}}$. Scattering matrix Z, which represents the properties of single

scattering in the layer, are calculated as

$$Z = f_h Z_h + (1 - f_h) Z_c, \tag{2.11}$$

where Z_h and Z_c are scattering matrices of haze and cloud particles, respectively. The optical thickness of haze in the cloud layer τ'_h also can be calculated as

$$\tau'_h = \frac{f_h}{1 - f_h} \tau_c. \tag{2.12}$$

τ''_R can be calculated as

$$\tau''_R = \frac{f_R}{1 - f_R} \tau_p, \tag{2.13}$$

where f_R is the Rayleigh fraction, and $\tau_p = \tau_c + \tau'_h$. The definition of Rayleigh fraction is

$$f_R = \frac{k_{\mathrm{sca,R}}}{k_{\mathrm{sca,p}} + k_{\mathrm{sca,R}}}, \tag{2.14}$$

where $k_{\mathrm{sca,R}}$ is the scattering coefficient of Rayleigh scattering, and $k_{\mathrm{sca,p}} = k_{\mathrm{sca,c}} + k_{\mathrm{sca,h}}$. The values of f_R were 0.043, 0.025, and 0.033 at λ =365nm in Hansen and Hovenier (1974), Kawabata et al. (1980), and Braak et al. (2002), respectively. Assuming $\tau_c = 30$ at this wavelength, which is consistent with *in situ* measurements [Esposito et al. (1983), Ragent et al. (1985)], τ''_R calculated from these values lead the altitude of the bottom of the cloud layer around 50km. Taking this into account, we fixed $f_R = 0.015$ at 438nm, which corresponds to $f_R = 0.03$ at 365nm.

2.3.2 Latitudinal profile of upper haze and cloud top altitude

Spatial variations in 930-nm polarization maps primarily come from the latitudinal distribution of haze. We assume a simple latitudinal distribution model as shown in figure 2.10. Hereafter we call the region of latitude be-

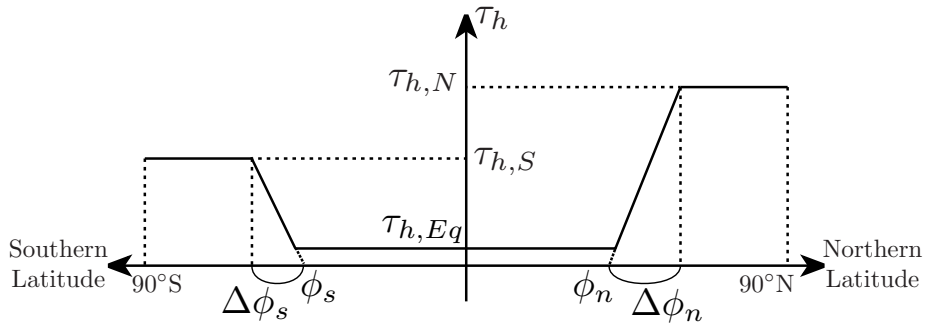

Figure 2.10: Latitudinal distribution of upper haze. Latitudinal distribution of upper haze is linear slope at the boundary latitude ϕ_n and ϕ_s, and constant between them. $\Delta\phi_n$ and $\Delta\phi_s$ are the width of the slope.

tween ϕ_n and $-\phi_s$ "Equatorial region", and other polar side regions "Northern polar region" and "Southern polar region". From latitude of ϕ_n $(-\phi_s)$ to $\phi_n + \Delta\phi_n$ $(-\phi_s - \Delta\phi_s)$, we call this "transition region", optical thickness of upper haze is assumed to linearly increase to $\tau_{h,N}$ and $\tau_{h,S}$. Figure 2.11 illustrates the differences of patterns for different width $(\Delta\phi)$ of transition region.

Spatial variations in 438-nm polarization maps come from the altitude of each layer's top. It is known that the cloud top altitude decreases with latitude from around 50° to the poles. In order to simulate this fact, we assumed simple model similar to the latitudinal distribution of the optical thickness of the haze layer as shown in figure 2.12. In this model, the boundary latitude, at which the cloud tops start lowering, ϕ_n and ϕ_s, and the width of the transition $\Delta\phi_n$ and $\Delta\phi_s$ are the same with those in figure 2.10.

In the analysis of IR data, as above mentioned, we assumed that the effect of Rayleigh scattering can be neglected, thus, $\tau_R = \tau'_R = \tau''_R = 0$. We firstly determine f_h and $\tau_{h,Eq}$ on equatorial region by analyzing the regions

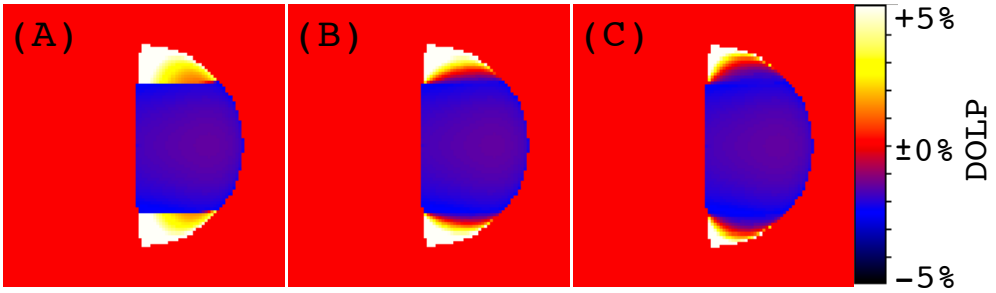

Figure 2.11: Differences of polarization maps by latitudinal distribution of upper hazes. (A) $\Delta\phi = 0°$, (B) $\Delta\phi = 20°$, (C) $\Delta\phi = 50°$. $\phi = 40°$ for (A), (B), (C)

near intensity equator (between $-15°$ and $+15°$) because such regions appear to be free from upper haze. Secondly, we adopt deduced f_h to both polar regions. Although f_h in the polar regions may not be the same as that of the equator, this treatment may be practical. The reason being that contributions from haze particles mixed in the cloud may well be masked by stronger polarizations of the upper haze if it is optically thick. If the upper hazes on polar regions are thin, hence the polarizations is not dominated by upper hazes, then we may simply re-adjust the value of f_h after comparing polarization maps.

The computed points are selected to include the best fit parameters in the range by considering the previous studies and test calculations. Maximum f_h and $\tau_{h,Eq}$ were 0.065 and 0.02 in PVO observations [Kawabata et al. (1980)], and maximum $\tau_{h,N}$ and $\tau_{h,S}$ were 0.30 during thick-haze period in 8 years from the beginning of the PVO mission [Sato et al. (1996)]. These can be thought to be the limitation of the points in theoretical calculations. Computation points of $\phi_n, \phi_s, \Delta\phi_n$, and $\Delta\phi_s$ are determined from the test calculations, and are confirmed to be consistent with the boundary latitude of

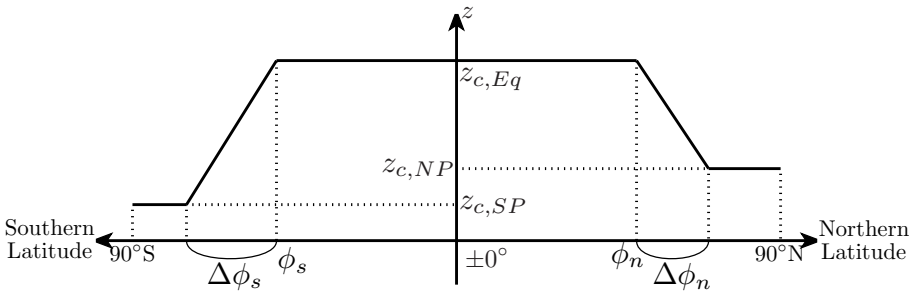

Figure 2.12: Latitudinal distribution of each layer top. $z_{c,Eq}$ is the cloud top altitude for equatorial region, $z_{c,NP}$ $z_{c,SP}$ are the cloud top altitude for North and South pole, respectively. Between latitude $\phi_n(\phi_s)$ and $\phi_n + \Delta\phi_n(\phi_s + \Delta\phi_s)$, the cloud top altitude decreases from $z_{c,Eq}$ to $z_{c,NP}(z_{c,SP})$ linearly.

Table 2.3: Range of calculated parameters for IR model

	f_h	$\tau_{h,Eq}$	$\tau_{h,N}$	$\tau_{h,S}$	ϕ_n [°]	ϕ_s [°]	$\Delta\phi_n$ [°]	$\Delta\phi_s$ [°]
start	0.000	0.00	0.00	0.00	31	31	10	10
end	0.060	0.03	0.30	0.30	49	49	30	30
step	0.005	0.01	0.01	0.01	3	3	5	5

the bright polar caps seen in UV images and previous polarimetric studies[cf. Lee et al. (2015), Kawabata (1981)]. The calculated points are listed in table 2.3.

2.3.3 Theoretical calculations for polarization map and disk-averaged DOLP

We generated theoretical polarization maps calculating I and Q for corresponding pixels in images considering local scattering geometries as

$$\mu \equiv \cos\theta = \frac{\sqrt{R^2 - (x^2 + y^2)}}{R}, \tag{2.15}$$

$$\mu_0 \equiv \cos\theta_0 = \mu\cos\alpha + \frac{x\sin\alpha}{R}, \tag{2.16}$$

$$\cos(\phi - \phi_0) = \frac{\mu\mu_0 - \cos\alpha}{\sqrt{(1-\mu^2)(1-\mu_0^2)}}, \tag{2.17}$$

$$\sin(\phi - \phi_0) = \frac{y\sin\alpha}{R\sqrt{(1-\mu^2)(1-\mu_0^2)}}, \tag{2.18}$$

where x and y are the horizontal and vertical coordinate of a point on the planetary disk, viewed from infinity with apparent radius R in pixel unit; θ_0 and ϕ_0 are zenith and azimuth angles for incident light; θ and ϕ are those for emergent light, as shown in figure 2.13 [after Kawabata (1981)]. The x-axis is taken to be the intensity equator, and the limb of the planet is assumed to be located on the positive domain of x. Disk-averaged DOLP were calculated by taking summations of I and Q for the whole planetary disk.

2.3.4 Point-spread functions to fit the "observed" polarization maps

Generally, we cannot get infinitely sharp image but get to some extent blurred image by observing a point source with an optical instrument, because the light is affected by several factors, such as diffraction in the instrument and atmospheric seeing. Such effects appear also in imaging of an disk object like Venus. How does the image spread can be described by functions called point-spread function (PSF). By convolving ideal images with a PSF, we

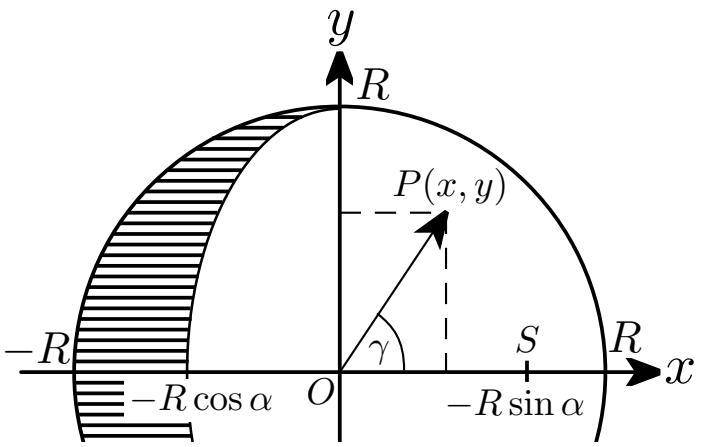

Figure 2.13: A schematic illustration of a planetary disk observed at phase angle α with apparent radius R. An observer is assumed to be located at long distance which can be regarded as infinity. The origin is taken at the center of disk. The point S on the x-axis corresponding to the intensity equator is sub-solar point. The terminator is located at $x = -R\cos\alpha$ on the intensity equator.

can reproduce the blurred images. Since patterns of polarization maps are affected by such effects, so knowing appropriate PSF is important in evaluating theoretical and observational polarization maps. In this subsection, we examine HOPS images and determine PSF. The blurring of images in ground-based observations is dominated by atmospheric seeing rather than instrumental factors, so hereafter we assume the source of the blurriness is due to atmospheric seeing.

Blurring of images is most commonly approximated with a Gaussian function;

$$f(x;\sigma) = \frac{1}{\sqrt{2\pi\sigma^2}} \exp\left(-\frac{x^2}{2\sigma^2}\right). \tag{2.19}$$

σ in this equation is the index of the size of PSF. While a Gaussian PSF well

describes "time averaged" seeing effects, the short-integrated Venus images "without time averaging" likely require a different shape of PSF. Therefore, we tested a "modified Lorentzian distribution function" in the following form as well:

$$f(x; a, \gamma) = \frac{C}{(x^2 + \gamma^2)^a}, \tag{2.20}$$

where γ is the size of PSF, a is the index of sharpness, and C is the constant of normalization. Figure 2.14 compares the differences of the shape among Gaussian function and modified Lorentzian distribution functions with several parameters.

First of all, we compared these 2 functions by adopting them to polarization standard stars, which can be regarded as point source. Figure 2.15 is an example which compares the best-fit functions to the radial profile of the standard star HD154445 (R.A.: $17^h05^m32^s.1$, Dec.: $-00°53'32''$, Visual magnitude: 5.62), which shows the modified Lorentzian distribution function makes a good fit, and actually the sum of the squared residuals is 15% smaller for modified Lorentzian distribution function. We tested for other stars and found that the sum of the squared residuals is always smaller in case of modified Lorentzian distribution function than Gaussian function. We can say that Lorentzian distribution function works better as the PSF.

We performed the similar process for Venus images to verify the adequacy of the modified Lorentzian distribution function and obtain appropriate PSF. To avoid possible contamination from the polar hazes, we examined limb profiles only near the intensity equator ($\pm 15°$) to determine the PSF (either Gaussian or Lorentzian, and the size of PSF). A synthetic image is generated with a "cloud only" model (described in the below) which is then blurred by a PSF with an assumed seeing size. After subtracting observed images, we evaluated the standard deviations of the residual intensities. Such analysis

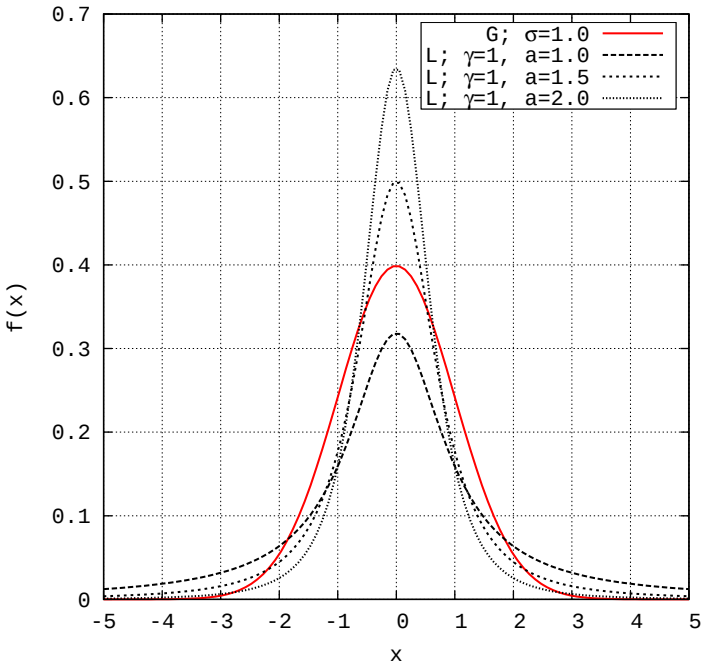

Figure 2.14: A comparison of Gaussian function and modified Lorentzian distribution functions with several parameters. "G" and "L" in the legend indicate Gaussian function and modified Lorentzian distribution function, respectively. Compared with Gaussian function, modified Lorentzian distribution functions are sharper. The sharpness can be varied by a.

is repeated to cover a wide range of σ or (γ, a). A combination of parameters which minimizes the standard deviation is chosen to best describe the PSF at the time of observation. Figure 2.16 compares the minimum standard deviations obtained from Gaussian and modified Lorentzian distribution functions.

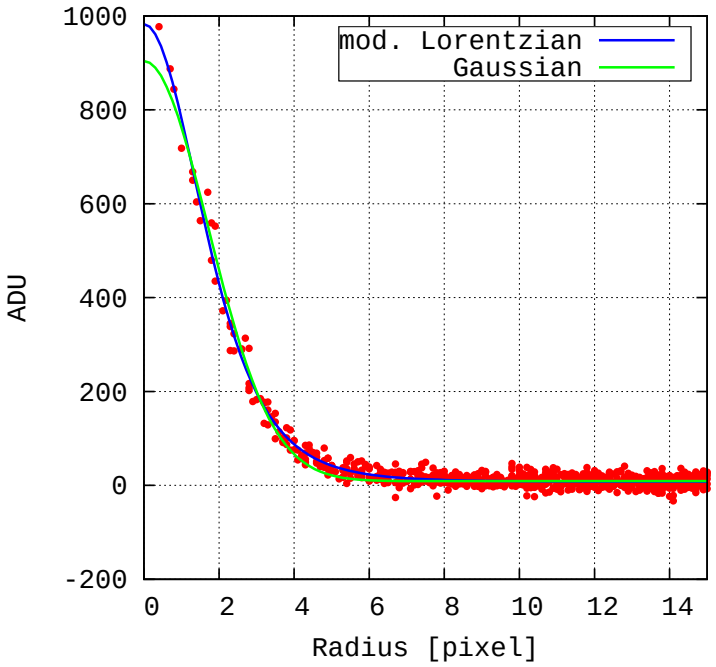

Figure 2.15: A comparison of best fit functions. The red points are the intensity of the standard star HD154445, measured from its center of gravity. The blue and green curves are the best fit for modified Lorentzian distribution and Gaussian functions, respectively. Modified Lorentzian distribution function can reproduce well the shape of the peak and tail than Gaussian function.

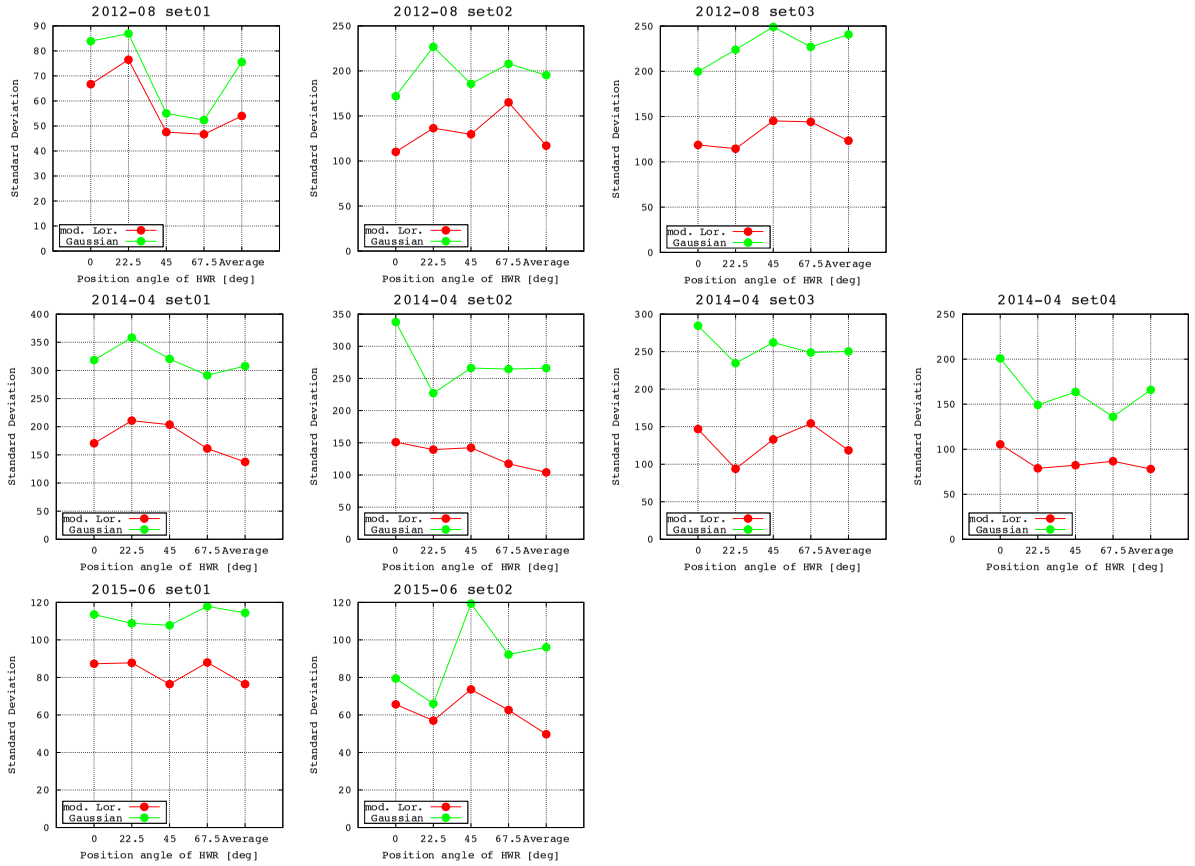

Figure 2.16: Comparisons of minimum standard deviations for Gaussian and modified Lorentzian distribution function. The minimum values of standard deviations are always smaller for modified Lorentzian distribution function than Gaussian function, which indicate the better reproducibility of the modified Lorentzian distribution function.

In any case, the standard deviations are smaller for modified Lorentzian functions. Figure 2.17 is the example of a comparison in adopting two functions to images.

The values of the standard deviation themselves are larger than those of annulus area (~ 20), which may be due to the incompleteness of the assumption of PSF and model settings in making synthetic images. But it is almost impossible to obtain complete PSF for variable atmospheric seeing because of its large randomness, so here we use the most reproductive parameters as appropriate PSF.

Figure 2.18 is a compilation of the set of γ and a in modified Lorentzian distribution functions, which indicates temporal variations of the PSF. We use these values to reproduce the blurred images in making synthetic polarization maps.

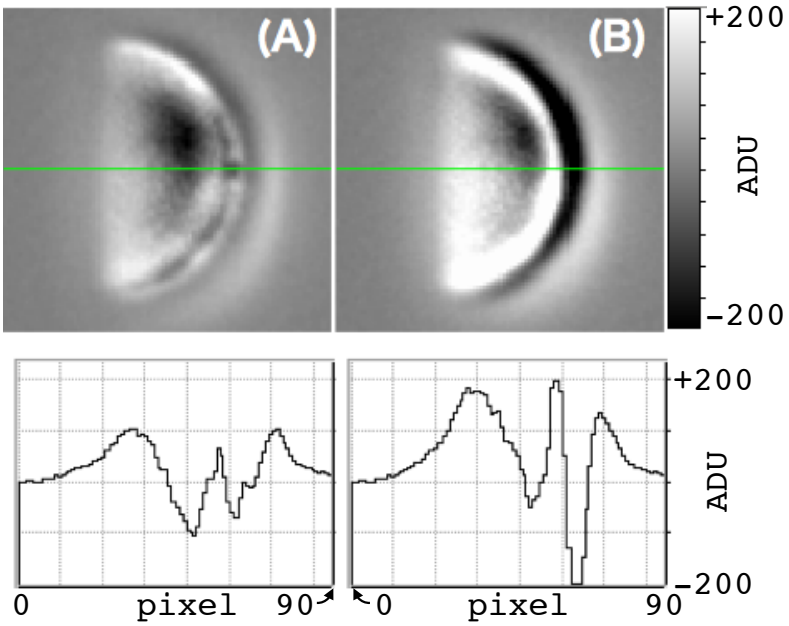

Figure 2.17: The difference between Gaussian function and modified Lorentzian distribution function as PSF. The upper images are the observed subtracted observed images blurred model images. The left is the result of modified Lorentzian distribution function with $a = 1.5, \gamma = 3$, the right is the result of Gaussian function with $\sigma = 4.2$. The lower plots are the intensities at the cross section on the intensity equators indicated with green lines in upper images.

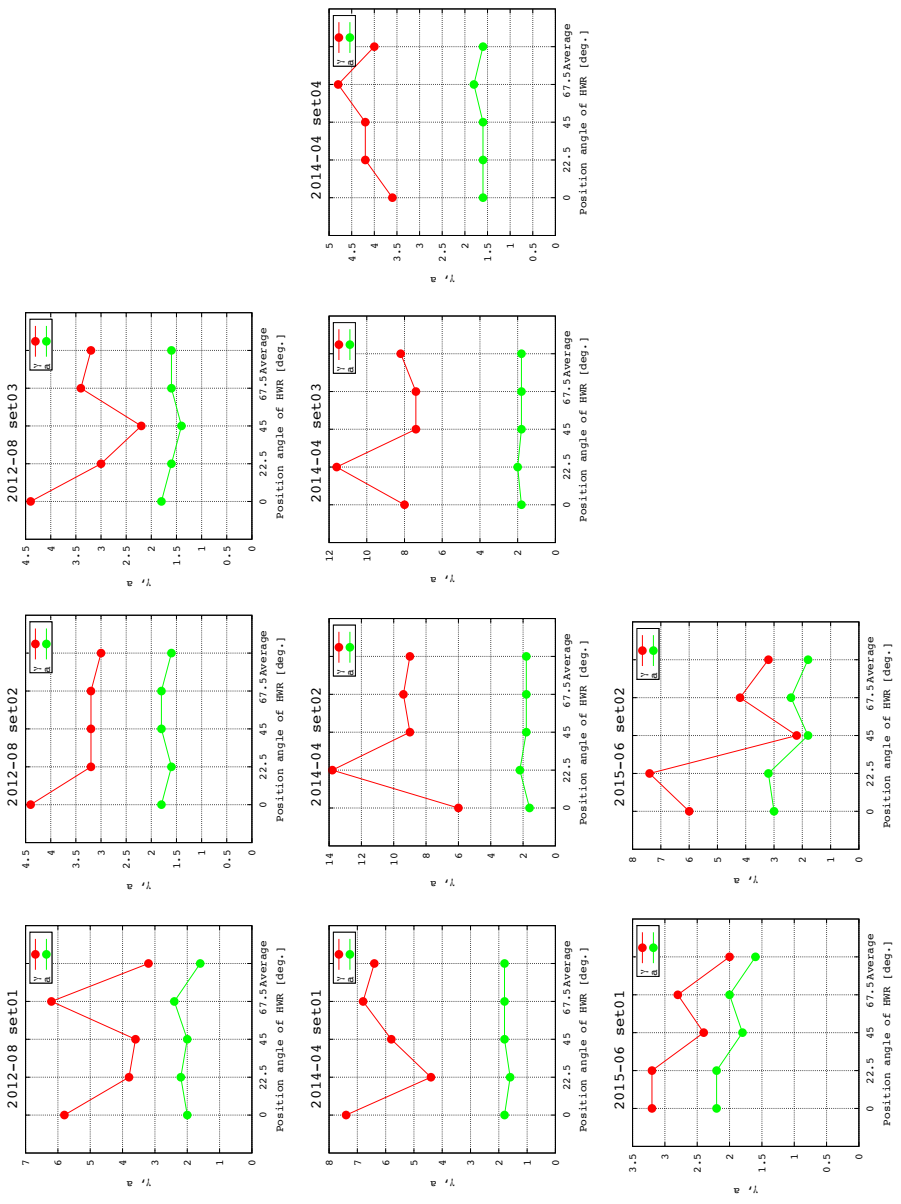

Figure 2.18: Temporal variations of γ and a. The values of γ a are obtained for images taken at the position angles of half wave retarder plate $\phi = 0°$, $22.5°$, $45°$, and $67.5°$. "Average" labels in the rightmost tics are the values for averaged images, not averages of the set of γ and a.

2.4 Evaluation of theoretical calculations

We evaluated the theoretical polarization maps by calculating means of squared residuals (MSR) described as

$$MSR = \sum_{i=1}^{N} \frac{(p_i^o - p_i^m)^2}{N}, \tag{2.21}$$

where N is the number of pixels, p_i^o and p_i^m are DOLP at i-th pixel in polarization maps of observations and models, respectively. The best fit parameters are determined by evaluating following conditions;

- $|P_m - P_o| \equiv \Delta P < P_e = P_{\rm th} + P_{\rm obs}$
- minimize MSR

where P_m and P_o are disk-averaged DOLP of models and observations, and P_e is the error range of disk-averaged DOLP. P_e can be considered as superposition of theoretical error $P_{\rm th}$ and observational error $P_{\rm obs}$. We discuss these two kinds of errors in the following subsections.

2.4.1 Errors in theoretical calculations

We performed sensitivity tests for the fixed parameters in the cloud model, in order to estimate the errors in theoretical calculations. Tested parameters are effective radius $r_{\rm eff}$, effective variance $v_{\rm eff}$, and refractive index n_r of cloud and haze particles. The range of test calculations are based on Sato et al. (1996). For cloud particles, the error ranges of the parameters are $r_{\rm eff}$=1.05 $\pm$ 0.1μm, $v_{\rm eff}$=0.07$\pm$0.02, and n_r=1.43$\pm$0.01. For haze particles, these are $r_{\rm eff}$=0.25$\pm$0.05μm, $v_{\rm eff}$=0.17$\pm$0.1, and n_r=1.43$\pm$0.01.

First of all, we show the results for the variations of cloud particle properties in figure 2.19. The curves in the figure are phase angle dependence

of disk-integrated polarizations corresponding to each parameter. We used cloud-only model, f_h=0 and τ_h=0, in order to consider the variations of cloud particle parameters themselves. In figure 2.19 (A), we can find almost no sensitivity around phase angle $\sim 80°$ for $r_{\rm eff}$of the cloud in a range of nominal value of 1.05 $\pm$ 0.05μm. There are several reports that there occasionally appears slightly larger particles called mode 2' with radius of 1.2μm. But cloud particles with $r_{\rm eff}$=1.25μm don't make large differences, which means that we cannot sense such differences from polarizations at this wavelength and phase angle. On the other hand, from figure 2.19 (B) and (C), there can be seen relatively large differences of polarizations with the variations of $v_{\rm eff}$and n_r of the cloud particles around phase angle $\sim 80°$. The differences of polarizations to the nominal model are around 0.1%, which can be regarded as the theoretical errors caused by cloud particle properties.

Secondly, we show the results for the variations of haze particle properties in figure 2.20 in the same way as figure 2.19. For simplicity, we take $\Delta\phi = 0°$ and $\phi = 50°$ in the latitudinal profile of upper haze, which is the same model with Kawabata (1981), and f_h=0.040 as a typical value of haze fraction. We can find differences of DOLP $\sim$ 0.1% for n_r (figure 2.20 (C)) around phase angle 80°, which can be regarded as the theoretical errors. On the other hand, there are considerable differences for $r_{\rm eff}$and $v_{\rm eff}$(figure 2.20). This large differences are due to the single scattering properties of haze particles. Figure 2.21 compares the polarizations caused by haze particles with effective radius of haze particles $r_{\rm eff}$=0.20, 0.25, and 0.30μm. When the effective radius is small compared with observing wavelength, the phase angle dependence of polarizations tends to be closer to that of Rayleigh scattering as show in figure 2.4. This is why such large positive polarizations are caused by smaller particles as $r_{\rm eff}$=0.20μm. This effect appears in the variations of $v_{\rm eff}$ because

these are the indexes of the width of a particle size distribution. Figure 2.22 compares the phase angle dependence of polarizations for optical thickness of upper haze $\tau_h$with $r_{\rm eff}$=0.20, 0.25, and 0.30μm. We can not distinguish the difference of the combination of τ_h and $r_{\rm eff}$ just with the value of the polarization. For example, ($r_{\rm eff}$, τ_h) = (0.2μm, 0), (0.25μm, 0.1), (0.3μm, 0.23) indicate similar polarization degrees $\sim -2.8\%$ at phase angle 90°. In order to avoid this problem, we have to continuously perform observations at several phase angles to pick up feature of the phase angle dependence of polarizations. But in such case, it takes half of synodic period ($\sim$292days) to obtain data in full range of phase angle, which makes us unable to distinguish phase angle dependence of polarizations from temporal variations of $r_{\rm eff}$and $v_{\rm eff}$. Sato et al. (1996) reported that the properties of haze particles were stable with $r_{\rm eff}$=0.25μm during about 8 years of Pioneer Venus mission, so we assumed that the radius of haze particle had not changed during our observation period. From the discussion above, we consider the errors from the variations of haze particle properties 0.1%.

Another possible source of theoretical error is the variation of the single scattering albedo of the cloud. In this study, we fixed this value to 0.99923, which is calculated assuming the effective radius $r_{\rm eff}$ in the particle size distribution equals to 1.05μm. However, if there are differences in it, the single scattering albedo can be changed. For example, the single scattering albedo is 0.99917 for $r_{\rm eff}$=1.2μm, and is 0.99931 for $r_{\rm eff}$=0.9μm. Such differences can make differences in theoretical values for cloud only model of about 0.02% in polarization degrees, which is relatively smaller than those obtained from sensitivity test above. So, finally, we take $P_{\rm th} = 0.2\%$.

2.4.2 Errors in observations

The possible sources of error from observations are

- the uncertainty of instrumental polarizations,
- the effect of atmospheric seeing to aperture photometry, and
- the uncertainty of the sky values.

The uncertainty of the instrumental polarizations can be thought to be negligible, because the standard deviation within the considered area is on the order of 10^{-4}% to the intensities of the object, which cannot make considerable effects to the polarization degrees.

In order to examine the effect of atmospheric seeing, we measured the intensities of the light leaking out of aperture and into annulus regions. The effect of the atmospheric seeing was considered by blurring synthetic images of Venus disk with radius of 27 pixels and phase angle of 70° (nearly corresponding to the situation of April 2014 observations). The PSF, the combinations of a and γ in modified Lorentzian distribution function, was adopted to images corresponding to the position angles of a half wave retarder. The values were taken from the measured values of April 2014 set01 data, because the atmospheric seeing in this period was worse than others, which can be thought as the worst case. The measured intensity in aperture region and annulus region were 98.9% and 0.04% to the true intensity in average, respectively (worst case is 98.0% and 0.1%). By using resultant values, the effect of the atmospheric seeing in the aperture photometry was found to be on the order of 10^{-5}% in polarization degrees, which is negligible compared to other observational errors.

The most considerable source of observational error is the uncertainty of the sky values. We measured standard deviation of each annulus region, and

take this into account in the derivation process of polarization degrees like

$$I_{\mathrm{r}}(\phi) = I_{\mathrm{obj}}(\phi) - d\sigma_{\mathrm{r}}(\phi), \tag{2.22}$$

where r is the kind of rays (replaced with "e" or "o" in equation 2.3), and ϕ is the position angle of half wave retarder plate, σ is the standard deviation of the count in annulus region, and d is the factor to determine whether σ is added or subtracted or done nothing, thus $d = \pm 1, 0$.

We calculate the differences between nominal polarization ($d = 0$ for all) and other polarizations for $3^8 = 6561$ patterns of combinations of $\phi = 0, 22.5°, 45°$, and $67.5°$, r (e and o), and $d = \pm 1$ and 0 (3 patterns of d for 8 data obtained at 4 position angle for 2 kinds of rays). Figure 2.23 shows histograms of the calculated polarizations. Then we calculate the standard deviations for all the polarizations and use them as the observational errors P_{obs}. The values of P_{obs} differ for observation set each other, which are listed in table 2.4.

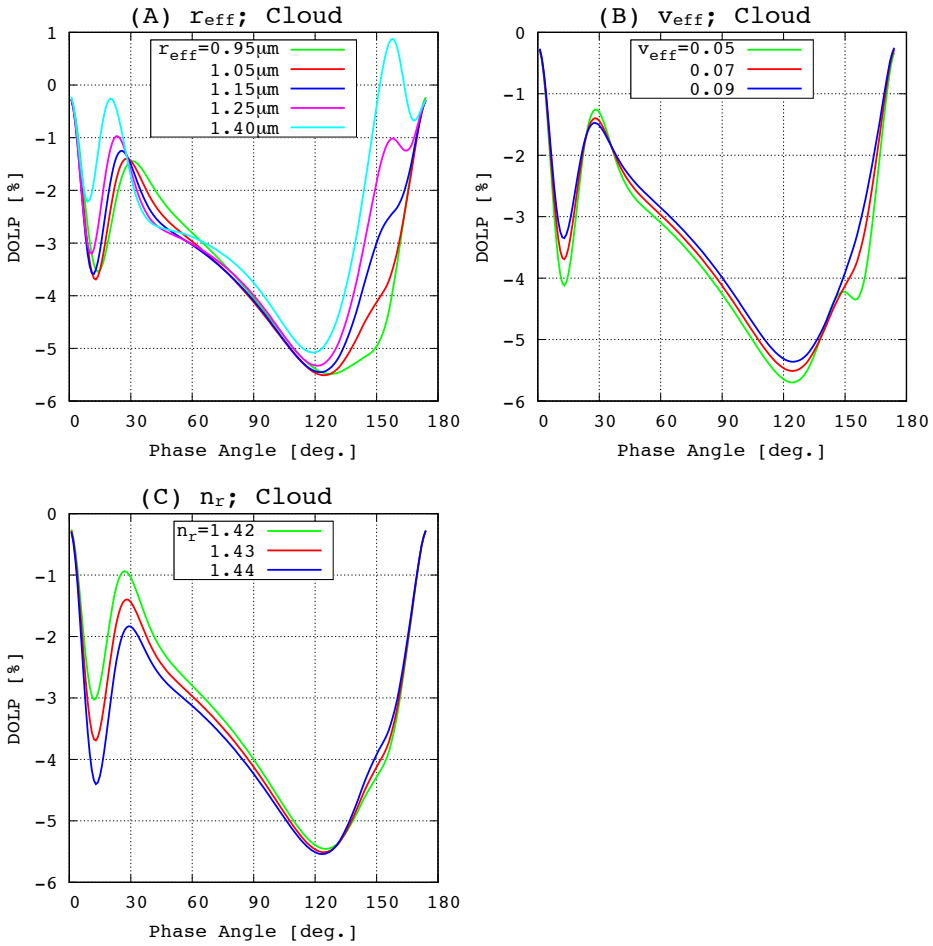

Figure 2.19: Sensitivity tests for cloud parameters for cloud-only model. Figure (A) is for effective radius r_{eff}, (B) is for effective variance v_{eff}, and (C) is for refractive index of the particles.

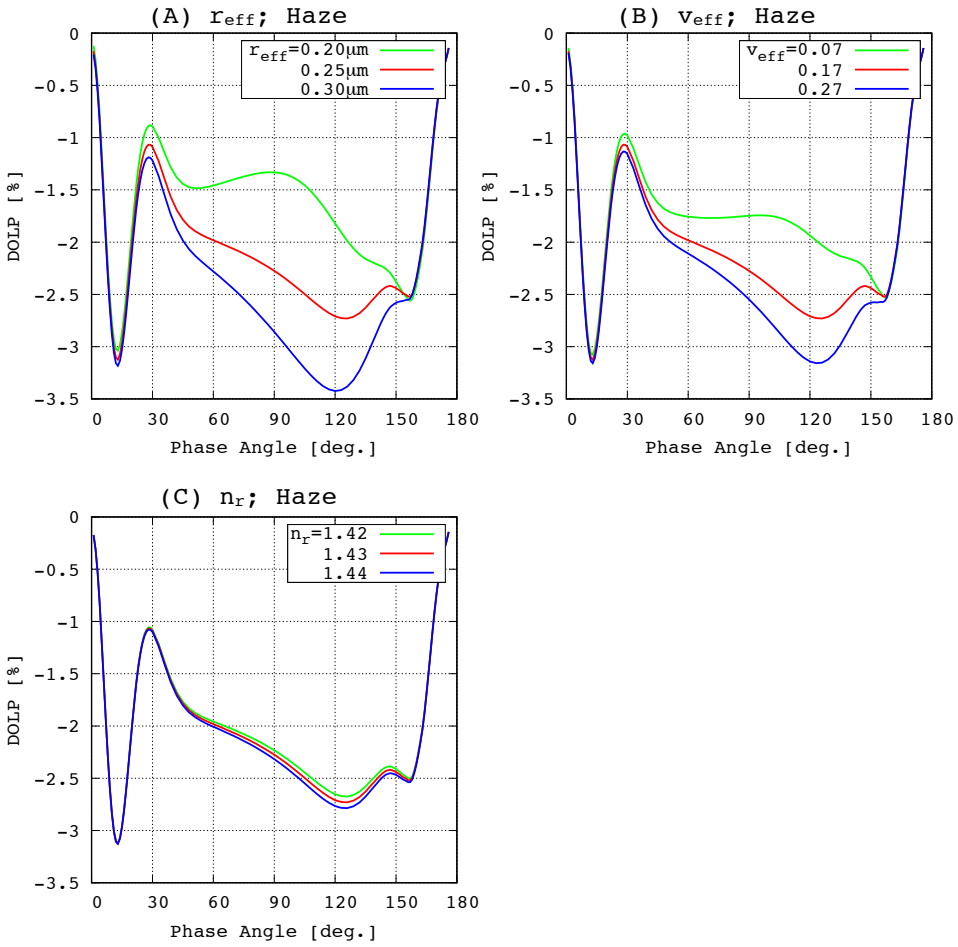

Figure 2.20: Sensitivity tests for haze parameters. (A), (B), and (C) are the same with figure 2.19, but for haze particles.

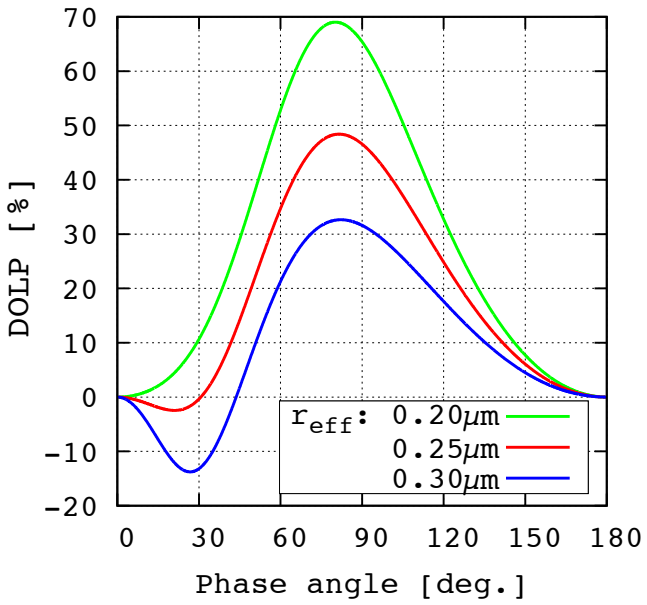

Figure 2.21: Single scattering polarizations for r_{eff}=0.20, 0.25, and 0.30μm. The polarizations for r_{eff}=0.20μm are similar to these of Rayleigh scattering as shown in figure 2.4.

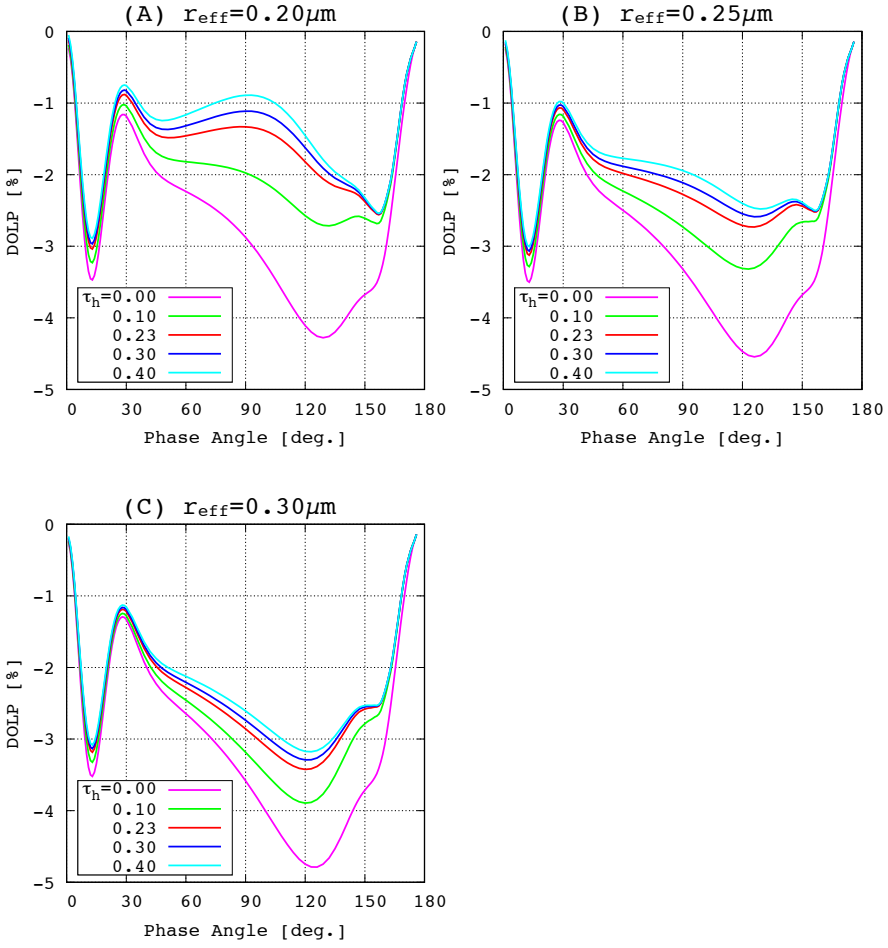

Figure 2.22: $r_{\rm eff}$ and τ_h dependence of polarizations. Although the polarizations at certain phase angle only cannot make us to distinguish the difference of $\tau_h$and $r_{\rm eff}$, but if we observe polarizations for wide range of phase angles, we can do it. In that case, the data can include the temporal variations of them.

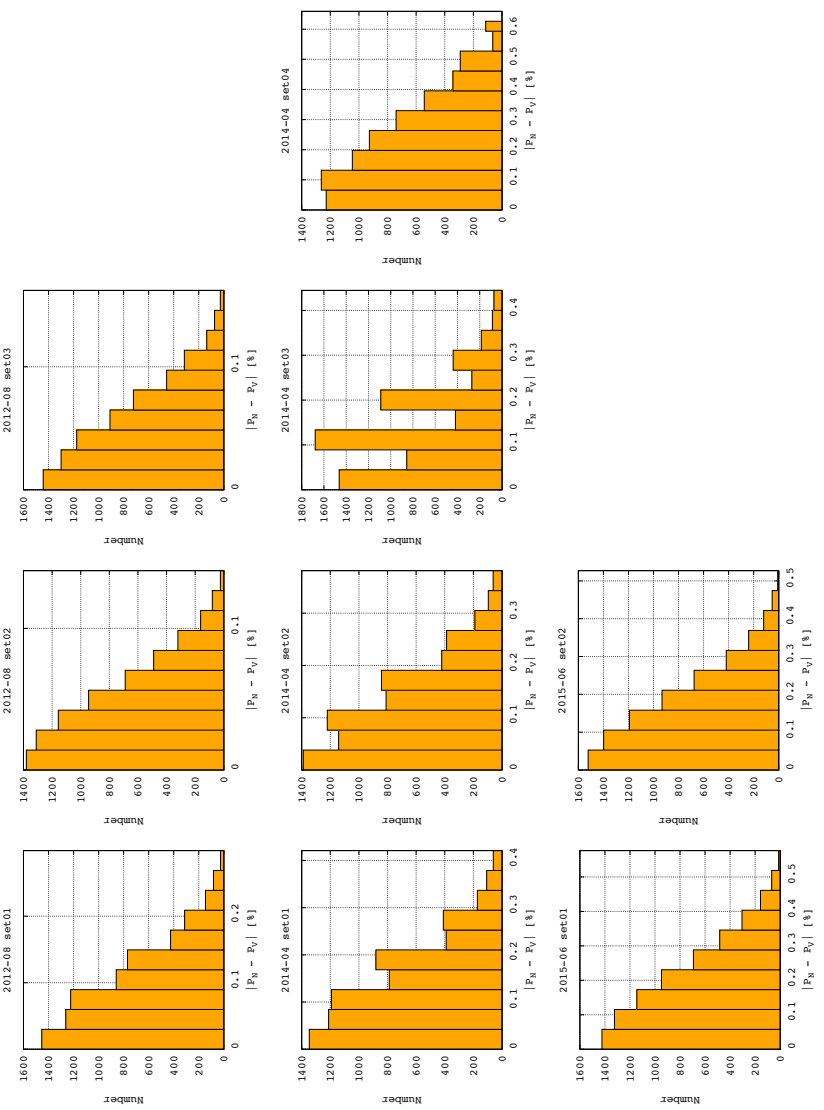

Figure 2.23: Histograms of the residuals of polarizations for uncertainties of the sky counts. The width of bins is one-tenth of the maximum of residuals.

Table 2.4: Observational errors.

Year and Moth	set	P_{obs} [%]
2012 August	1	0.10
	2	0.05
	3	0.06
2014 April	1	0.16
	2	0.14
	3	0.16
	4	0.25
2015 June	1	0.20
	2	0.17

Chapter 3

Result

3.1 IR (930nm)

3.1.1 Observed disk-integrated DOLP and polarization maps

Observed disk-averaged DOLP and polarization maps of IR date are listed in table 3.1 for selected data set (filtered by the seeing size). Since 4 images included in each observational set were acquired within a few minutes, we do not need to consider the effect of cloud motion called "super rotation" of Venusian atmosphere ($\sim$ 4 days of rotation period).

Table 3.1: Properties of observations and results for IR data. Date and time is described in universal time. ϕ_0: latitude of sub-observer point, $R_{\rm a}$: apparent radius, $R_{\rm i}$: radius in images, $P_{\rm disk}$: disk-averaged DOLP.

Year-Month	Date	time	set	$\alpha[^\circ]$	$\phi_0[^\circ]$	$R_{\rm a}[''']$	$R_{\rm i}$ [pix.]	$P_{\rm disk}[\%]$
2012-August	22	18:48	1	85.4	+2.39	10.9	33.1	−2.13
	22	19:38	2	85.4	+2.39	10.9	33.1	−2.29
	23	19:35	3	84.8	+2.33	10.8	32.8	−2.03
2014-April	23	1:43	1	74.1	−0.10	9.1	27.5	−3.19
	23	2:25	2	74.1	−0.10	9.1	27.5	−3.36
	24	2:19	3	73.6	−0.06	9.0	27.4	−3.24
	25	0:48	4	73.2	−0.01	8.9	27.1	−3.10
2015-June	1	8:29	1	86.8	−2.73	11.1	33.7	−3.64
	1	8:52	2	86.8	−2.73	11.1	33.7	−3.63

Figure 3.1 compares disk-averaged DOLP in our observations with previous observations taken from Kawabata et al. (1980). Observed DOLP in August 2012 are higher than 1960's by about 1.5%, which is likely caused by abundant sub-micron hazes in polar regions. Note that there are also some observations of such high polarization in 1960's data, which could probably be attributed to temporal increases of upper hazes.

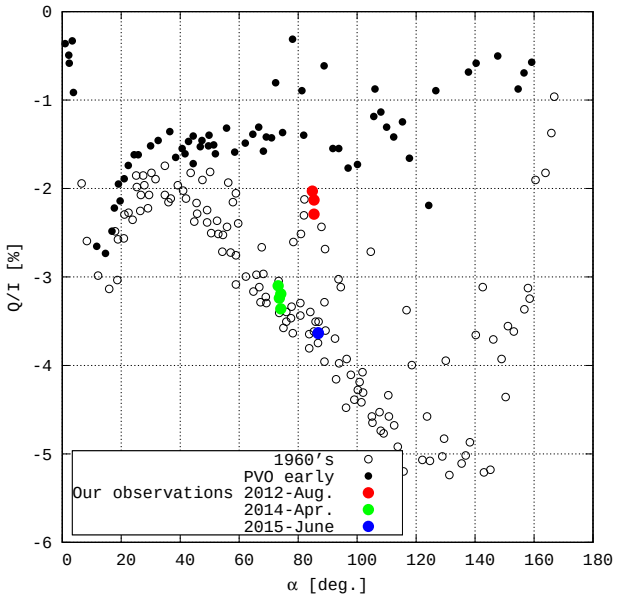

Figure 3.1: Comparisons of observed DOLP with previous studies. "1960's" and "PVO early" indicated by black circles are taken from Kawabata et al. (1980), both are disk-averaged DOLP. "PVO early" data are affected by positive polarizations from hazes, between phase angle of 45° and 160°. Our data in 202-Aug. also indicate such existence of hazes in the atmosphere. Note that 1960's data around $\alpha \sim 80°$ might also indicate the existence of hazes.

Figure 3.2 is the summary of the obtained polarization maps of IR data. A strong enhancement of positive polarization in the polar regions is obvious

in August 2012 data, while the same regions in other periods are all negative polarization. Polarization seen in the low to middle latitude regions in August 2012 is slightly higher in positive than those in other periods. Since the positive polarization is caused by haze particles, such temporal variations in polarization should indicate an decrease of the optical thickness of the hazes from 2012 to later years.

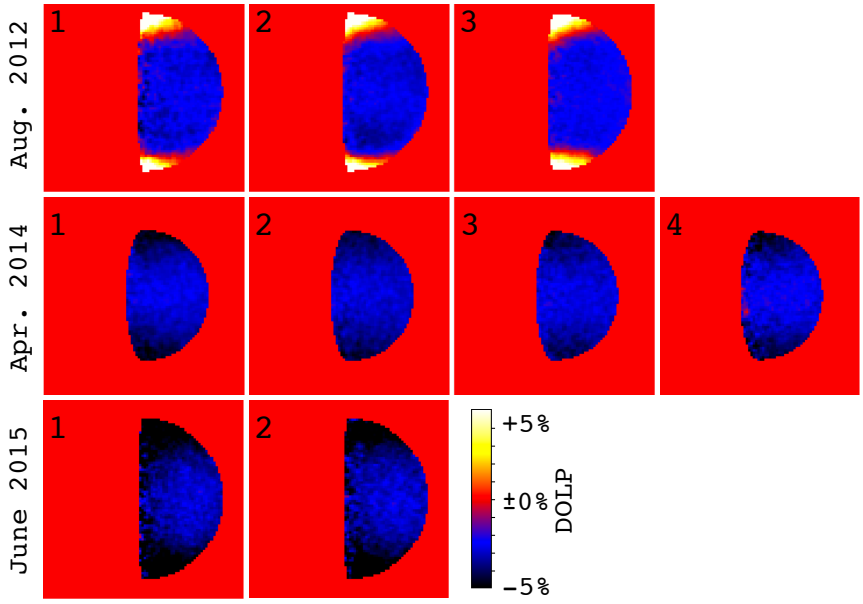

Figure 3.2: A summary of obtained polarization maps at 930nm wavelength. The numbers on the top left corner are the sequential set number of observations. Cloud particles generate negative polarization at this wavelength, while haze particles generated negative polarizations. The positive polarizations on the polar regions in August 2012 indicate the existence of upper hazes.

3.1.2 Comparisons with models

Figure 3.3 compares theoretical DOLP with observations. The color contour is the value of MSR of polarization maps, and squares filled with 4 colors are the residuals of disk-integrated DOLP between observations and theoretical calculations (ΔP). The best-fit parameters are obtained as the points, in the parameter space, that satisfy $\Delta P < P_e$ and minimize the value of MSR at the same time.

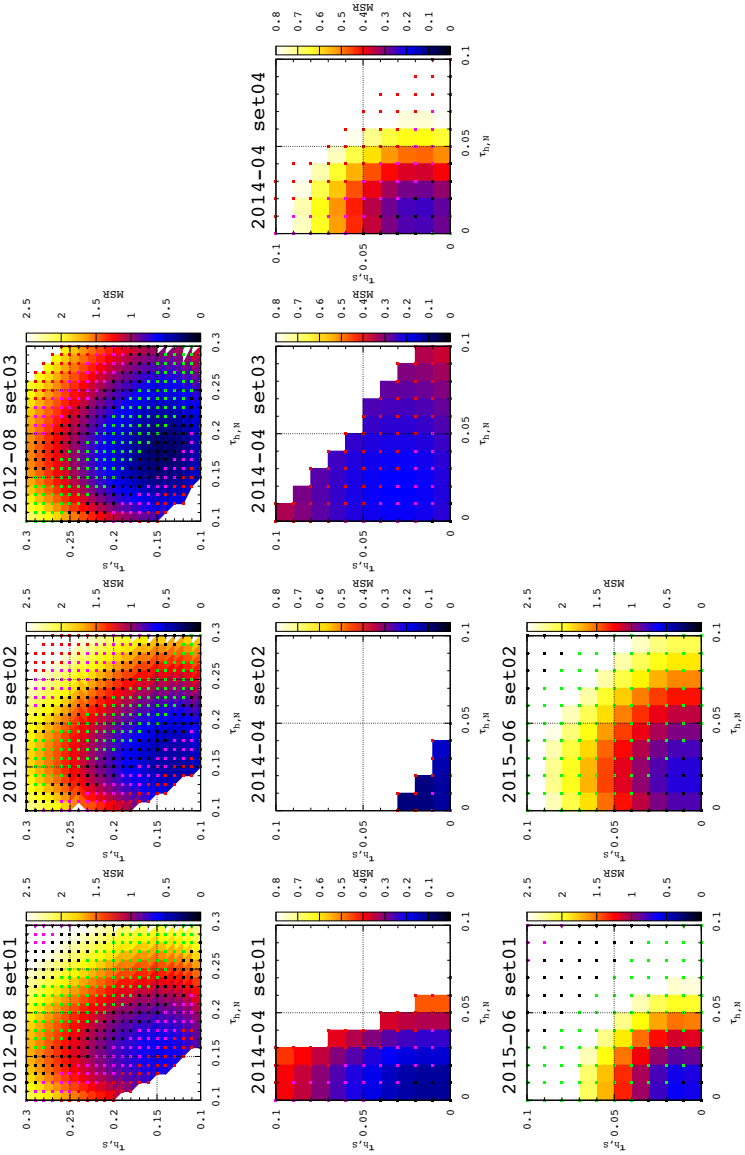

Figure 3.3: Compariaons of integrated DOLP and polarization maps of observations with theoreticals. The contour maps here are the maps including the best fit parameters of ϕ_n, ϕ_s, $\Delta\phi_n$, $\Delta\phi_s$. The colors of squares on the contours indicate the value of ΔP; Green: $\Delta P < P_e/4$, Black: $\Delta P < P_e/2$, Magenta: $\Delta P < 3P_e/4$, Red: $\Delta P < P_e$.

We summarize the best fit parameters in table 3.2. The averaged optical thickness of upper haze for North and South polar regions are about 0.15 in August 2012, 0.01 in April 2014, 0.01 for both in June 2015. The averaged value of the fraction of haze in the cloud f_h also decreased from 0.047 to 0.01 during this period. "Model No." in the table indicate the parameter set used in Blue analysis.

Table 3.2: Properties of observations and best fit values for IR model. The values in parenthesis are uncertainties in estimations.

Year-Month	Date	set	Model No.	f_h (± 0.005)	$\tau_{h,Eq}$ (± 0.01)	ϕ_n [°] (± 3)	$\Delta\phi_n$ [°] (± 5)	$\tau_{h,N}$ (± 0.01)	ϕ_s [°] (± 3)	$\Delta\phi_s$ [°] (± 5)	$\tau_{h,S}$ (± 0.01)
2012-August	22	1	1	0.045	0.00	34	30	0.15	40	25	0.15
	22	2	2	0.040	0.00	34	30	0.16	46	10	0.13
	23	3	3	0.055	0.00	37	30	0.18	40	15	0.14
2014-April	23	1	4	0.025	0.00	31	15	0.01	43	30	0.01
	23	2	5	0.005	0.01	31	30	0.01	31	10	0.02
	24	3	6	0.015	0.02	46	20	0.02	40	25	0.03
	25	4	7	0.020	0.01	31	15	0.01	31	30	0.02
2015-June	1	1	8	0.010	0.00	46	15	0.01	46	20	0.01
	1	2	9	0.010	0.00	43	30	0.02	43	30	0.01

3.2 Blue (438nm)

3.2.1 Observed disk-integrated DOLP and polarization maps

Observed disk-averaged DOLP and polarization maps of IR date are listed in table 3.3 for selected data set. "Model No." in the right column correspond to the Number listed in table 3.2, which is the set of the model parameters used for Blue analysis.

Table 3.3: Same as table 3.1, but for Blue data.

Year-Month	Date	time	set	$\alpha[^\circ]$	$\phi_0[^\circ]$	$R_{\rm a}[''']$	$R_{\rm i}$ [pix.]	$P_{\rm disk}[\%]$	γ	Model No.
2012-August	22	18:56	1	85.4	+2.39	10.9	33.2	−0.88	2.8	1
	22	19:44	2	85.4	+2.39	10.9	33.2	−0.67	2.6	2
	23	19:30	3	84.8	+2.33	10.8	32.9	−0.60	3.2	3
2014-April	24	2:13	1	73.6	−0.06	9.0	27.4	−0.25	5.2	6
	25	0:39	2	73.2	−0.01	8.9	27.1	−0.10	5.0	7
	25	0:40	3	73.2	−0.01	8.9	27.1	−0.01	5.0	7
2015-June	1	8:39	1	86.8	−2.73	11.1	33.8	−0.86	2.0	8
	1	9:00	2	86.8	−2.73	11.1	33.8	−1.14	2.2	9
	1	10:23	3	86.8	−2.73	11.1	33.8	−1.25	2.4	9

Figure 3.4 is the summary of the obtained polarization maps of Blue data. Strong positive polarization can be seen on the both polar region in August 2012 and June 2015, while such strong contrast cannot be seen over the disk in April 2014. This indicates that the cloud top altitude of the polar region in April 2014 is not so lower than those of August 2012 and June 2015.

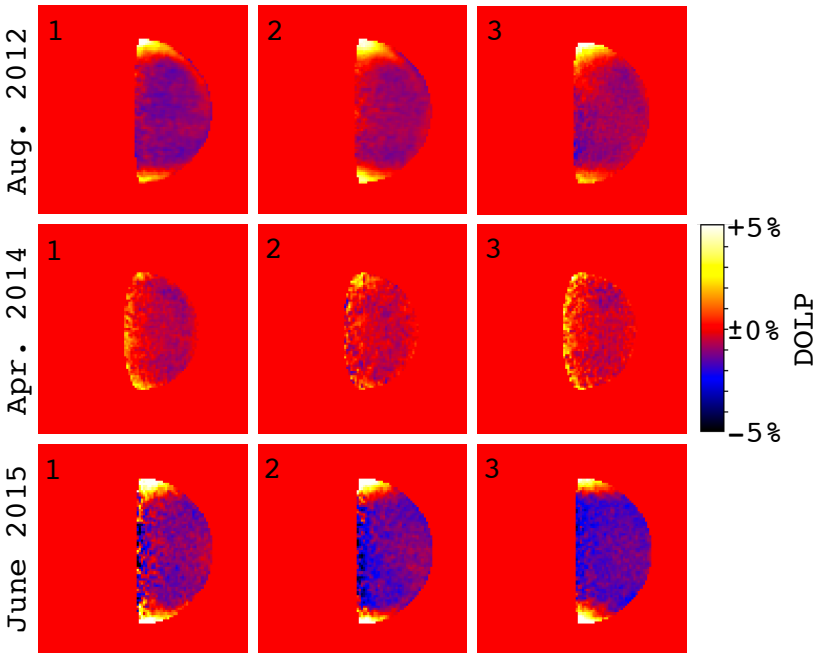

Figure 3.4: Same as figure 3.2, but for Blue data. Positive polarization can be generated by Rayleigh scattering from molecules in upper atmosphere, which is the indication of the layer top altitude.

Chapter 4

Discussion

Our observations in the period of 2012 to 2015 indicate significant decrease in the abundance of sub-micron haze particles in both polar regions. The optical thickness of the upper haze decreased by a factor of 10, and such a rapid decrease was also observed by PVO in the first 1000 days of its mission period (Kawabata et al. (1983)). The speed of the decrease is comparable with their study. Such variation in the upper atmosphere can affect the vertical profile of the solar heating. Crisp (1986) carried out model calculation which vary aerosol optical thickness at 71km level. His calculations show that the near-infrared solar heating increases above this level, and decreases bellow, when the optical thickness is doubled. On the other hand, when the optical thickness is halved, the opposite variation on the solar heating rate occurs. This means that the upper atmosphere can be more heated when the upper haze is abundant, as early period of PVO mission and August 2012.

The boundary latitude, distinguishing hazier polar region from less hazier low latitudes, is found around 40° with a transition band of which width is 30°. Kawabata (1981) analyzed phase angle dependence of polarization degrees observed with OCPP onboard PVO, and estimated that the boundary

which is equivalent to our transition band was about 50°. Although their boundary is like a step function (no transition band), our result is consistent with their result. This is also consistent with the boundary latitude of the bright-dark contrast seen in UV images (Lee et al. (2015)).

This latitude corresponds to the latitude where the cloud top altitude begins to lower towards the pole (e.g. Lee et al. (2012), Ignatiev et al. (2009)). Braak et al. (2002) pointed out that there were correlations between cloud top altitude and the number density of upper haze, proportional to optical thickness, from polarimetric data by OCPP. They proposed 2 hypotheses about this correlation; (a) haze particles are distributed uniformly in certain altitude over whole latitude, thus lowering of the cloud top leaves relatively more of sub-micron particles above the cloud, (b) since the polar region is the region where the atmosphere converges by meridional circulation (diverges in the lower latitudes), haze particles or other materials may be accumulated in this region.

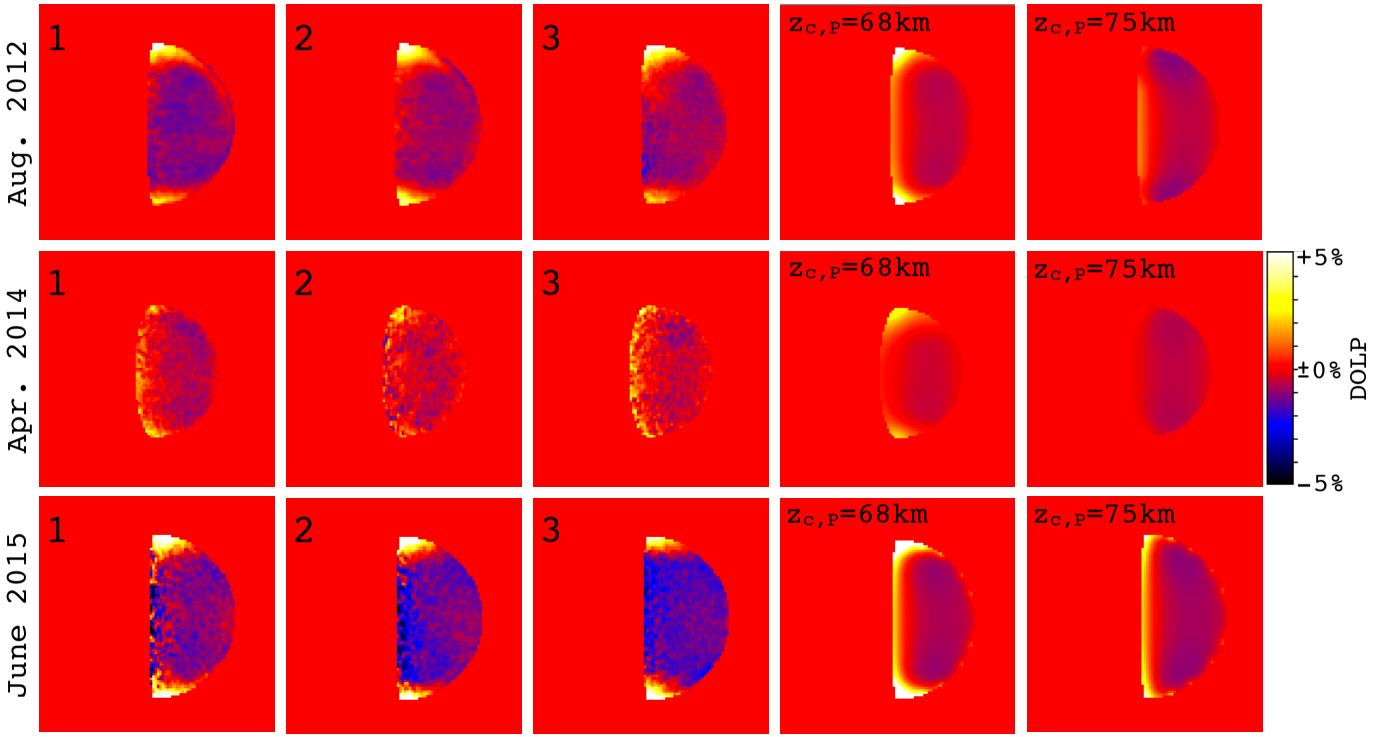

Figure 4.1: Comparisons of polarization maps of observed and theoreticals at 438nm wavelength. The theoretical maps on the 2 rightmost columns are calculated for different $z_{c,NP}$ and $z_{c,SP}$ of 68km and 75km. The cloud top altitudes of equatorial regions are fixed to $z_{c,Eq}$=75km. The positive polarizations at this wavelength are generated by Rayleigh scattering.

Firstly, we note on Braak et al.'s hypothesis (a). From our observations, it seems that there are not always correlations between the optical thickness of upper haze and cloud top altitude. By examining the HOPS Blue data (λ =438nm) to which Rayleigh scattering has significant influences, we can obtain rough estimates of the cloud top altitudes. We have generated "reference" polarization maps for 2 different cloud top altitudes of polar regions, 68, and 75 km, as shown in figure 4.1. The cloud top altitude of equatorial regions are fixed to $z_{c,Eq}$=75km. The polarization degrees in the equatorial region of observations are slightly different from those of theoretical maps; observed polarizations in equatorial regions are negatively strong compared with theoreticals. These differences may be caused by the differences of single scattering albedo of the cloud particles at this wavelength. Single scattering albedo contributes to the strength of polarizations because strong absorption reduces the effect of the multiple light scattering. The single scattering albedo in this study is calculated from the typical value of spherical albedo of Venus. However, absorption in this wavelength region can be variable due to the spatial variability of absorber in the atmosphere. Therefore, if the single scattering albedo at this time is lower than the value used in this study, hence absorption is stronger, polarizations should be negatively stronger. Although there can be such differences of the single scattering albedo, we can qualitatively compare patterns in the polarization maps due to cloud top variations.

In the polarization maps of August 2012 and June 2015, the polar regions exhibit positive polarization despite the fact that polarization at 438 nm generated by cloud particles should be negative. This positive polarization is caused by the Rayleigh scattering, which translates to the column abundance of molecular gas above the cloud top. Therefore, relatively strong

positive polarization, seen in both August 2012 and June 2015, indicates that the cloud top altitude is relatively lower than low to middle latitude regions. In contrast, the polarization map of April 2014 looks uniform over the entire disk. By comparing with theoretical maps, the cloud top altitude near the polar regions are not so lower than other areas. In order to roughly estimate the cloud top altitude from Blue data, we compare the differences of the polarizations of polar regions (over 50° in latitude) to equatorial regions (below 15° in latitude). For example, for April 2014 data, the differences of the polarization of north polar region to equatorial region in the model of $z_{c,p}$=68km and 75km, ΔP_{68} and ΔP_{75}, are 1.46% and 1.18%, respectively. On the other hand, such a difference for observations, ΔP_{obs}, is 1.2%. By considering the ratio of increments of altitude and the differences of polarizations, we obtained 74.5km as the altitude reproducing the value of ΔP_{obs}, which is comparable with the altitude of equatorial region. In the same manner, we obtain 62km and 64km as the cloud top altitude for August 2012 and June 2015, respectively. The situation in June 2015 is that the optical thickness of the haze is small while the cloud top altitude is low, which indicates that there could be time when lower cloud top altitude (positive polarization at 438 nm) and smaller haze optical thickness (as obtained from 930-nm data) co-exist. Therefore, the hypothesis (a) of Braak et al. (2002) may not always be true.

Hypothesis (b), adevection and accumulation, is a possible explanation for our observations. Actually the pole-ward winds are observed by cloud-tracking technique by Rossow et al. (1990), which is considered as an upper part of meridional circulation. However, since we don't have any ways to examine this hypothesis, we leave this hypothesis as a possible explanation of the temporal variation of the haze.

As the "cloud-top lowering" hypothesis does not work on all of our data, we need alternative ways to explain the variations of the optical thickness of hazes. Possible ways are to alter the vertical profile of haze or to simply increase/decrease the haze abundance for all altitudes. We now examine the former possibility. Optical thickness of the haze above the cloud can, in general, be estimated by knowing three quantities: (i) cloud top altitude, (ii) scale height of particles , and (iii) number density of haze particles at a reference altitude. For (i) and (ii), we refer to Lee et al. (2012). For (iii), we refer to the extinction coefficients for 80-km altitude as inferred from SPICAV/SOIR data (Wilquet et al. (2012)), For (iii), we also refer to Wilquet et al. (2012). Although these profiles are not exactly suitable for quantitative examination for the wavelength of our interest, we can qualitatively examine the behavior of those parameters. The optical thickness of upper hazes were calculated by integrating extinction coefficient $\beta(z)$ expressed as

$$\beta(z) = \beta_{80} \exp\left(-\frac{z-80}{H_a}\right), \tag{4.1}$$

where H_a is aerosol scale height, and β_{80} is the extinction coefficient at 80km altitude.

The dots in figure 4.2-(a) are the extinction coefficients, in figure 4.2-(b) are the cloud top altitudes, and in figure 4.2-(c) are the aerosol scale heights, respectively. These latitudinal profiles are fitted by quintic functions. Finally, we obtain figure 4.2-(d), the latitudinal profile calculated by using those equations. We call a constant term in the quintic function fitted to the cloud top altitude "nominal", whose value was about 68km. We allow this value to vary from 74km to 76km, somehow simulating the expected cloud top altitude for visible wavelengths. Computed results, of course, show that the optical thickness of the haze changes as the cloud top altitude changes in a similar way as Braak et al.'s hypothesis. However, we have already men-

tioned that the HOPS/Blue data indicate the period of lower cloud top and smaller haze optical thickness (June 2015). Therefore, our interest is whether another physical quantity, the aerosol scale height, could better explain our observations or not.

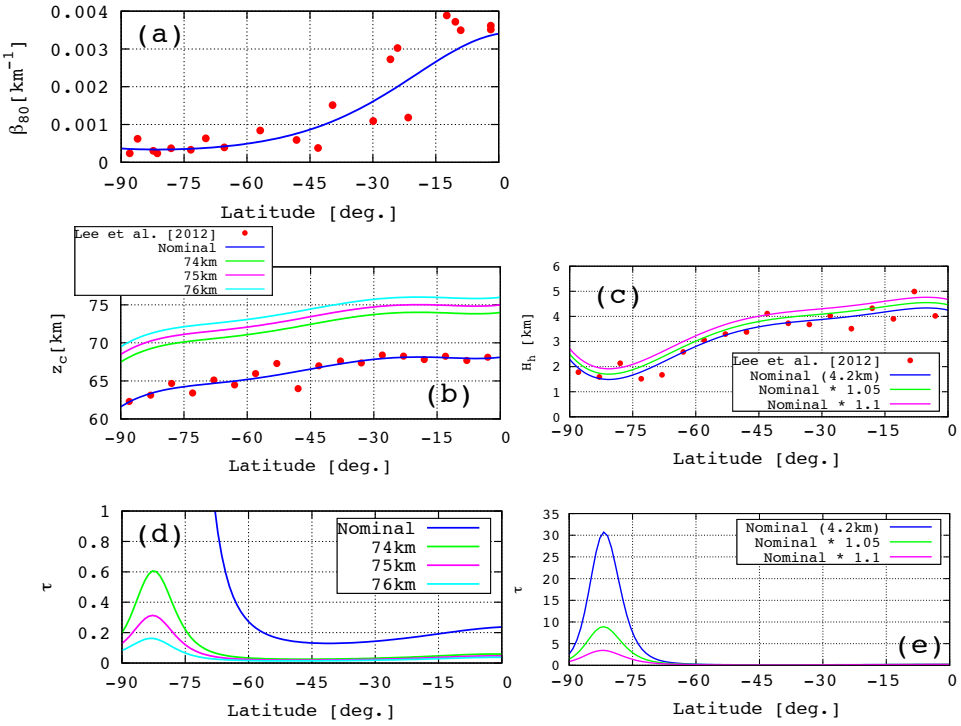

Figure 4.2: The parameters for examinations. Each figure is the latitudinal profile of (a)the extinction coefficient at 80km altitude (dots are taken from Wilquet et al. (2012)), (b) the cloud top altitude (dots are taken from Lee et al. (2012)), (c) the aerosol scale height (dots are taken from Lee et al. (2012)). (d) and (e) are calculated optical thickness using the latitudinal profiles of (b) and (c), respectively.

Figure 4.2-(e) shows the aerosol scale height dependence of the optical thickness. We changed the constant term in the fitted quintic function from

1.05 and 1.1 times of "nominal" value 4.2 km (4.4 km and 4.6 km). Corresponding to this small change in the scale height, the optical thickness varies on the order of magnitude. To examine how the aerosol scale height affects the haze mixing ratio in the cloud, we perform tests by fixing the aerosol extinction coefficient at 70 km altitude (cloud top) rather than 80 km of Wilquet et al. (2012). The scale height dependence of τ_h and f_h is obtained by assuming the extinction profile as an exponential function of the altitude. The definition of τ_h and f_h here are

$$\tau_h(H_h) = \int_{z_c}^{\infty} \beta_h(z, H_h) dz, \tag{4.2}$$

$$f_h(H_h) = \int_{z_u}^{z_c} \beta_h(z, H_h) dz, \tag{4.3}$$

$$\text{with } \beta_h(z, H_h) = B_h \exp\left(-\frac{z - z_c}{H_h}\right) \tag{4.4}$$

where z_c is the cloud top altitude (here z_c =70km), H_h is the scale height of haze particle extinciton, B_h is the extinction at cloud top altitude. z_u is the altitude where the optical thickness of the cloud becomes unity measured from z_c, which satisfies

$$\int_{z_u}^{z_c} \beta_c(z) dz = 1, \tag{4.5}$$

$$\text{with } \beta_c(z) = B_c \exp\left(-\frac{z - z_c}{H_c}\right) \tag{4.6}$$

where H_c is the scale height of aerosol (cloud) extinciton, B_c is the extinction of the cloud at cloud top altitude. The vertical profile is taken from Wilquet et al. (2012), by fitting $\beta_h(z)$ to the data acquired in September and October 2009 at 60°S latitude as a typical profile. We multiply B_h by 100, that is,

$$B_h = 100 B_{h,o} \tag{4.7}$$

in order to match the order of optical thickness at visible wavelengths, where $B_{h,o}$ is the original value taken in the fitting. We set the aerosol scale height

of cloud H_c=4km referring Lee et al. (2012), and the aerosol scale height of haze H_h as a function of the factor to H_c written as

$$H_h = xH_c. \tag{4.8}$$

Figure 4.3-(a) is the vertical profile of the extinction for cloud and haze used in this simulation. For haze profile, some examples are displayed for several value of x. Figure 4.3-(b) shows the behavior of τ_h and f_h with the variation of H_h calculated under this condition. According to this figure, f_h does not change over some range, while τ_h increases with H_h. This means that the simultaneous decrease of τ_h and f_h deduced from our observations cannot be explained by the variations of cloud top altitude and/or aerosol scale height. However, when we use 20 as a factor in equation 4.7 instead of 100, both optical thickness of upper haze and fraction of haze in the cloud decrease for any x. This indicates that the simultaneous decrease of these parameters is caused by the decrease of the amount of the haze itself.

Esposito et al. (1988) showed that there is also a long-term positive correlation between them with correlation coefficient 0.8, which means the global amount of SO_2 declines, so should be the production of haze aerosols (figure 4.4-(A)). Using the relation between the optical thickness of the upper haze and SO_2 abundance, we estimated the SO_2 abundance during our observation period. The linear function between the optical thickness of upper haze for $\lambda = 930$nm $\tau_{930\mathrm{nm}}$ and SO_2 abundance at 70km altitude f_{SO_2} was found to be

$$f_{SO_2} = 242\tau_{930\mathrm{nm}} + 0.449[\mathrm{ppb}], \tag{4.9}$$

with correlation coefficient 0.82 (figure 4.4-(B)). We estimated SO_2 abundance by adopting our results to this function, and plotted in figure 4.5, which shows the temporal variation of SO_2 abundance observed by Pioneer

Venus and Venus Express. This figure shows that a long-term decreasing trend in SO_2 abundance from 2007. Our results are consistent with this trend if this has been continued after the mission period of Venus Express. The decrease of optical thickness of upper hazes which our HOPS observations revealed could possibly be attributed to the consequence of decrease of SO_2 abundance.

We can raise the solar activity as the possible external factor of such variation of SO_2 abundance in the Venusian atmosphere, because the photodissociation of SO_2 occurs with short wavelength UV radiation (63-220nm) [Zhang et al. (2012)], which strongly varies with the solar activity. Figure 4.6 shows the sunspot relative number observed in National Astronomical Observatory Japan, Mitaka, which is the index of the strength of the solar activity. Several phenomenon, which can be related to the solar activity, are reported or observed. Dollfus et al. (1979) reported from ground-based polarimetric observations in 1958 that the polarizations on Venusian polar regions indicated positive, which should be explained with the existence of the sub-micron sized particles, hazes. This period corresponds to around the solar maximum indicated with label "A" in figure 4.6. The label "B" corresponds to, of course, the abundant hazes observed by PVO in 1979. The label "C" also indicates the solar maximum around 1993, when the SO_2 abundance was observed to be slightly increased as seen in figure 4.5. Around 2003 labeled with "D", although there is no obvious observations about variation of SO_2 abundance and optical thickness of haze, the solar activity may have affected to the Venusian atmosphere. Figure 4.7 shows the integrated flux of Venus with LASCO C3, which indicates a change of the brightness of Venus, brighter until 2003, then darker from 2005. It is unclear why this change happened, this can indicate a variation of the atmospheric

state of Venus. Finally, label "E", corresponding to the solar maximum, is our study, abundant haze on polar regions. Actually solar storms hit the Venus around this period, and the star tracker of VEx went down in March 2012 (`http://sci.esa.int/jump.cfm?oid=50665`).

Lee et al. (2015) showed that the contrast of the bright polar caps to the darker equatorial region seen in UV images decreased until 2009, and then gradually increased. This year corresponds to the solar minimum, and they also pointed out the possibility of the solar activity to such variations.

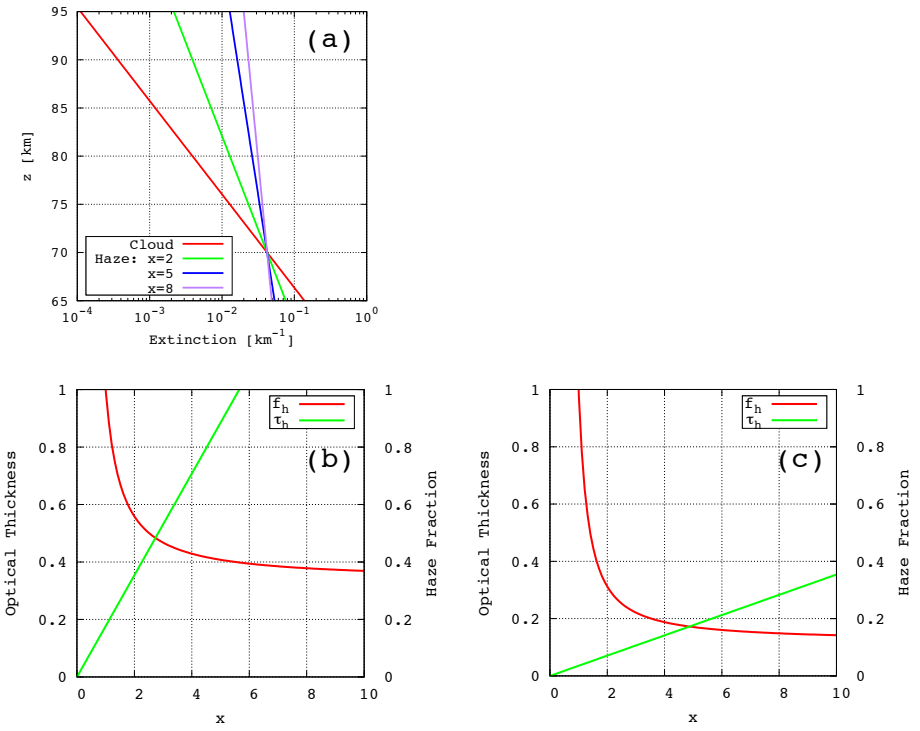

Figure 4.3: The simulations of the aerosol scale height dependence of τ_h and f_h. (a) The vertical profile of the extinction of the cloud and haze. Several lines for haze is the examples for various value of x. (b)(c) The factor dependence of the optical thickness and fraction of haze. (b) is for $B_h = 100B_{h,o}$, and (c) is for $B_h = 20B_{h,o}$.

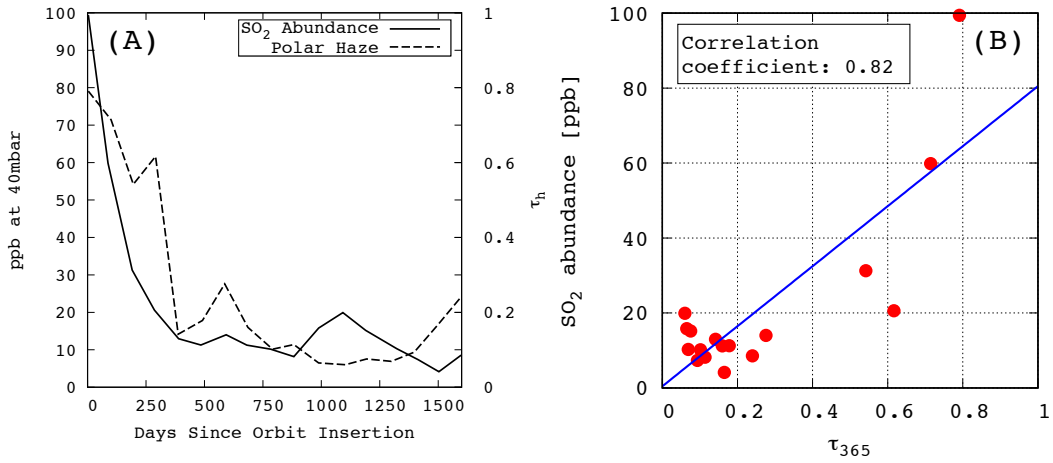

Figure 4.4: (A) Inter comparison between optical thickness of upper haze at $\lambda = 365$nm and SO_2 abundance during PVO mission period [After Esposito et al. (1988)]. (B) Scatter plot of optical thickness of upper haze (τ_{365}) and SO_2 abundance. Data points are taken from (A).

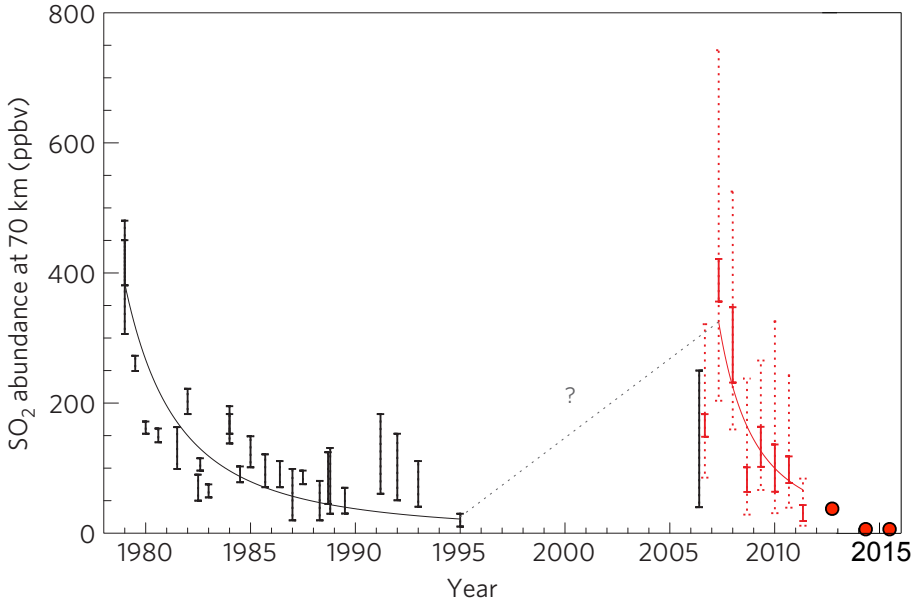

Figure 4.5: SO_2 abundance observed in PVO and VEx mission period [Marcq et al. (2013)]. Red circles are estimated value from equation 4.9 with obtained optical thickness of upper haze in this study.

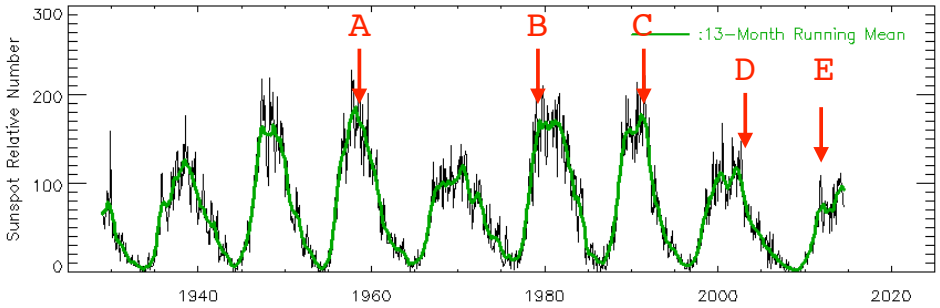

Figure 4.6: Sunspot relative number observed in National Astronomical Observatory Japan, Mitaka. This image is taken form `http://solarwww.mtk.nao.ac.jp/jp/solarobs.html`. The explanations about the indexes from A to E are described in the text.

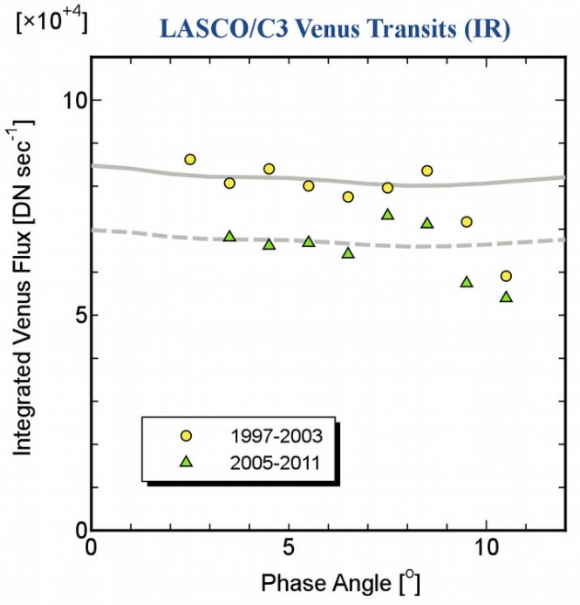

Figure 4.7: Phase angle dependence of the flux of Venus (Satoh et al. (2015)), which reflects the characteristics of the cloud and haze in the atmosphere.

Chapter 5

Conclusion

Through a 3-year ground-based polarimetric observation program, from August 2012 to June 2015 at phase angles ($\sim 80°$) best suited for polarimetry, we have detected a rapid decrease of the upper haze in Venus atmosphere. To overcome the blurring of images due to atmospheric seeing, the point-spread function is modeled with a modified Lorentzian function, and both disk-integrated polarization and two-dimensional polarization map are simultaneously analyzed. This analysis technique allows us to obtain the following results:

1. In 2012, the disk-averaged linear polarization at λ =930 nm was ~ -2.2 %, more than 1 % higher than in 2014 (~ -3.3 %) or in 2015 (~ -3.6 %). More neutral polarization in 2012 is interpreted as caused by a combination of negatively-polarizing clouds in the middle to low latitudes and positively-polarizing sub-micron hazes in the polar regions.

2. The equatorward boundary of polar haze exists around 40° (north or south). In poleward of this boundary, the optical thickness of upper haze at λ =930 nm are 0.15 for both the north and south. These

decreased to 0.01 for both polar regions by 2015.

In equatorward of the boundary (40° N to 40° S), the optical thickness of haze above the cloud is much smaller, 0.00, while the fraction of haze particles mixed in cloud layer is 0.047 in 2012. The fraction also decreased to 0.016 in 2014 and 0.010 in 2015.

3. The temporal variations of the cloud top altitude estimated from λ =438 nm data indicate that while the cloud top altitude in polar regions in August 2012 and June 2015 were lower than other latitudes, the cloud top altitude was relatively globally uniform in April 2014.

These findings challenge the "cloud lowering effect" hypothesis proposed by Braak et al. (2002): when the cloud top lowers, sub-micron particles shrouded in the cloud get exposed over the cloud, resulting in an increase of the optical thickness of upper haze. Our 2015 data obviously contradict this hypothesis: although the cloud tops in polar regions lowered in June 2015, the upper haze did not thicken. We examined the possibility of the variation of vertical profile of hazes. Although this model is capable of giving a large variability in the optical thickness of the upper haze, the model fails to change the fraction of hazes in the main cloud by a desired amplitude.

Therefore, decrease of hazes may be a consequence of lower aerosol production rate which may possibly be triggered by the decrease of SO_2 in the atmosphere reported with the Venus Express observations for a period from 2007 to 2012. Cloud and haze particles are thought to be H_2SO_4, produced from SO_2 via a chain of chemical reactions. This long-term decreasing trend, thus the decrease of the source of aerosol particles, can be the cause of decreasing of the optical thickness of haze.

We propose the relationships to the solar activity as a possible explanation for such variation of SO_2. Several phenomena, such as increases of haze and SO_2, seem to correspond to the solar maximum. The photochemical reactions, thus production of SO_2, might become active since the UV flux increase in solar maximum. In order to confirm the relations between solar activity and SO_2 or τ_h, long-term observations over several ten years are needed for the future.

After the end of Venus Express mission in 2014, Akatsuki, Japan's Venus orbiter, arrived at Venus and started observations in December 2015. The ultraviolet images (UVI) onboard Akatsuki has a SO_2-sensitive filter (283 nm) and will monitor the condition of the upper atmosphere of Venus in coming years. We expect to see what happens after the rapid decrease of the haze (never seen before) through coordinated observations of Akatsuki and ground-based polarimetry.

Acknowledgements

まずはじめに、5 年間研究指導にあたってくださった指導教員の佐藤毅彦教授に感謝を申し上げます。学部 4 年時に先生のもとを訪ね、大学院進学・卒業研究のテーマの相談に乗っていただき、偏光を使った観測の有効性を教えていただきました。そしてそれ以来、6 年に渡って偏光をテーマとした研究を続けてきました。大学院入学後も、観測・データ解析から科学的な思考、効果的な研究発表の仕方まで、あらゆる面で学ばせていただきました。この間に身につけたことは、研究のみならず今後の人生においてもきっと役に立てることができると感じています。「あかつき」の PI としてお忙しい中、最後まで博士論文執筆を支えていただき、深く感謝いたします。

この博士論文を書く上で欠かせない観測データの取得には、飛騨天文台 65cm 屈折望遠鏡の存在が欠かせません。65cm 望遠鏡の維持管理を献身的に行ってくださり、観測時にはサポートをしていただき、時には朝まで飲み明かした京都大学飛騨天文台の仲谷善一様、そして関係者の皆様にも深く感謝いたします。

また、博士論文審査の審査員を務めて下さった早川基教授、今村剛教授、阿部琢美准教授、生田ちさと准教授には、様々な角度からご指摘をいただき、この博士論文をより良いものにすることができました。特に予備審査時にいただいたご指摘により、解析において観測時の条件をより現実的に考慮し、より信頼出来る解析結果を得ることができたと思います。お忙しい中審査員をお引き受け頂き、感謝いたします。

宇宙科学研究所・惑星大気グループのポスドクの先輩方には、セミナーから日常での研究に関する話まで、様々な場面で大変お世話になりました。特に佐藤隆雄博士は私の研究状況を気にかけてくださり、相談をよくさせていただきました。自分の知識の至らなさを感じると同時に、この研究を進める上で何が必要なのかということも考えるきっかけを与えていただきました。

また、同研究所の秘書の皆様方には日常生活のサポートをしていただき、おかげで快適な研究生活を送ることができました。特に佐藤研秘書の木下留理子様、阿部研秘書の石川美穂様には、普段の生活で考えたり感じたりしたことまで聞いていただき、そのことがとても支えとなりました。

最後に、大学院進学を認め、陰ながら応援してくれた両親に感謝申し上げます。

Bibliography

Braak, C.J., de Haan, J.F., Hovenier, J.W.: Spatial and temporal variations of Venus haze properties obtained from Pioneer Venus Orbiter polarimetry. Journal of Geophysical Research **107**(E5), 1–13 (2002). doi:10.1029/2001JE001502

Chamberlain, J.W., Smith, G.R.: Interpretation of the Venus CO_2 Absorption Bands. Astrophysical Journal **160**, 755 (1970). doi:10.1086/150467

Crisp, D.: Radiative forcing of the Venus mesosphere. Icarus **514**(67), 484–514 (1986)

de Haan, J.F., Bosma, P.B., Hovenier, J.W.: The adding method for multiple scattering calculations of polarized light. Astronomy and Astrophysics **183**, 371–391 (1987)

Dollfus, A., Auriere, M., Santer, R.: Wavelength dependence of polarization. XXXVII. Regional observations of Venus. The Astronomical Journal **84**(9), 1419–1436 (1979). doi:10.1017/CBO9781107415324.004

Esposito, L.W., Knollenberg, R.G., Marov, M.I., Toon, O.B., Turco, R.P.: The clouds and hazes of Venus. In: Hunten, D.M., Colin, L., Donahue, T.M., Moroz, V.I. (eds.) Venus, pp. 484–564. University of Arizona Press, Tucson, Arizona (1983)

Esposito, L.W., Copley, M., Eckert, R., Gates, L., Stewart, A.I.F., Worden, H.: Sulfur dioxide at the Venus cloud tops, 1978—1986. Journal of Geophysical Research: Atmospheres **93**(D5), 5267–5276 (1988). doi:10.1029/JD093iD05p05267

Hansen, J.E., Hovenier, J.W.: Interpretation of the polarization of Venus. Journal of Atmospheric Sciences **31**, 1137–1160 (1974)

Hansen, J.E., Travis, L.D.: Light scattering in planetary atmospheres. Space Science Reviews **16**, 527–610 (1974). doi:10.1007/BF00168069

Hovenier, J.W., Mee, C.V.M.v.d., Domke, H.: Transfer of Polarized Light in Planetary Atmospheres. Kluwer Academic Publishers, The Netherlands (2004)

Ignatiev, N.I., Titov, D.V., Piccioni, G., Drossart, P., Markiewicz, W.J., Cottini, V., Roatsch, T., Almeida, M., Manoel, N.: Altimetry of the Venus cloud tops from the Venus Express observations. Journal of Geophysical Research E: Planets **114**(8), 1–10 (2009). doi:10.1029/2008JE003320

Imamura, T., Hashimoto, G.L.: Venus cloud formation in the meridional circulation. Journal of Geophysical Research **103**(E13), 31349–31366 (1998). doi:10.1029/1998JE900010

Kawabata, K.: Investigation of some of the principal geometric effects on planetary polarization. Moon and Planets **24**, 291–318 (1981). doi:10.1007/BF00897103

Kawabata, K., Sato, M., Travis, L.D.: Latitudinal and temporal variations of Venus polarization. In: Proceedings of the ISAS Lunar and Planetary Symposium 16, pp. 5–8 (1983). Institute of Space and Astronautical Science

Kawabata, K., Coffeen, D.L., Hansen, J.E., Lane, W.a., Sato, M., Travis, L.D.: Cloud and haze properties from Pioneer Venus polarimetry. Journal of Geophysical Research **85**(A13), 8129–8140 (1980). doi:10.1029/JA085iA13p08129

Kawata, Y.: Circular polarization of sunlight reflected by planetary atmospheres. Icarus **33**(1), 217–232 (1978). doi:10.1016/0019-1035(78)90035-0

Knibbe, W.J.J., DeHaan, J.F., Hovenier, J.W., Travis, L.D.: Analysis of temporal variations of the polarization of Venus observed by Pioneer Venus Orbiter. Journal of Geophysical Research **103**(97), 8557–8574 (1998)

Knollenberg, R.G., Hunten, D.M.: The microphysics of the clouds of Venus: Results of the Pioneer Venus Particle Size Spectrometer Experiment. Journal of Geophysical Research **85**(A13), 8039 (1980). doi:10.1029/JA085iA13p08039

Krasnopolskii, V.A., Parshev, V.A.: Photochemistry of the Venus atmosphere. In: Hunten, D.M., Colin, L., Donahue, T.M., Moroz, V.I. (eds.) Venus, pp. 431–458. University of Arizona Press, Tucson, Arizona (1983)

Lee, Y.J., Titov, D.V., Tellmann, S., Piccialli, A., Ignatiev, N., Pätzold, M., Häusler, B., Piccioni, G., Drossart, P.: Vertical structure of the Venus cloud top from the VeRa and VIRTIS observations onboard Venus Express. Icarus **217**(2), 599–609 (2012)

Lee, Y.J., Imamura, T., Schröder, S.E., Marcq, E.: Long-term variations of the UV contrast on Venus observed by the Venus Monitoring Camera on board Venus Express. Icarus **253**, 1–15 (2015)

Marcq, E., Bertaux, J.-L., Montmessin, F., Belyaev, D.: Variations of sulphur dioxide at the cloud top of Venus's dynamic atmosphere. Nature Geoscience **6**(1), 25–28 (2013). doi:10.1038/ngeo1650

Mishchenko, M.I., Travis, L.D., Lacis, A.A.: Scattering, Absorption, and Emission of Light by Small Particles. Cambridge University Press, Cambridge, UK (2002)

Moroz, V.I.: Stellar Magunitude and Albedo Data of Venus, pp. 27–35. University of Arizona Press, Tucson, Arizona (1983)

Ragent, B., Esposito, L.W., Tomasko, M.G., Marov, M.I., Shari, V.P.: Particulate matter in the Venus atmosphere. Advances in Space Research **5**, 85–115 (1985). doi:10.1016/0273-1177(85)90199-1

Rossi, L., Marcq, E., Montmessin, F., Fedorova, A., Stam, D., Bertaux, O. Jean Loup an d Korablev: Preliminary study of Venus cloud layers with polarimetric data from SPICAV/VEx. Planetary and Space Science **113-114**, 159–168 (2015). doi:10.1016/j.pss.2014.11.011

Rossow, W.B., Del Genio, A.D., Eichler, T.: Cloud-tracked winds from Pioneer Venus OCPP images. Journal of the Atmospheric Sciences **47**(17), 2053–2084 (1990). doi:10.1175/1520-0469(1990)047

Sato, M., Travis, L.D., Kawabata, K.: Photopolarimetry Analysis of the Venus Atmosphere in Polar Regions. Icarus **124**(2), 569–585 (1996). doi:10.1006/icar.1996.0231

Satoh, T., Enomoto, T., Sato, M.T.: Interannual Variability of Venus Albedo as Inferred from LASCO C3 Data. In: Proceedings of Japan Geoscience Union Meeting 2015 (2015). Japan Geoscience Union

Satoh, T., Kawabata, K., Yamamoto, N., Tenma, T., Akabane, T.: HOPS : Developement and the First-Light Observations of a New Imaging Polarimetry Instrument for the Planets. In: Proceedings of the ISAS Lunar and Planetary Symposium 34, pp. 146–149 (2001). Institute of Space and Astronautical Science

Seiff, A.: Appendix A; Models of Venus's atmospheric structure. In: Hunten, D.M., Colin, L., Donahue, T.M., Moroz, V.I. (eds.) Venus, pp. 1045–1048. University of Arizona Press, Tucson, Arizona (1983)

Tinbergen, J.: Astronomical Polarimetry. Cambridge University Press, Cambridge, UK (1996)

Tomasko, M.G., Doose, L.R., Smith, P.H., Odell, A.P.: Measurements of the Flux of Sunlight in the Atmosphere of Venus. Journal of Geophysical Research - Atmospheres **85**(80), 8167–8186 (1980). doi:10.1029/JA085iA13p08167

Wilquet, V., Drummond, R., Mahieux, A., Robert, S., Vandaele, A.C., Bertaux, J.L.: Optical extinction due to aerosols in the upper haze of Venus: Four years of SOIR/VEX observations from 2006 to 2010. Icarus **217**(2), 875–881 (2012). doi:10.1016/j.icarus.2011.11.002

Yung, Y.L., Demore, W.B.: Photochemistry of the stratosphere of Venus: Implications for atmospheric evolution. Icarus **51**(2), 199–247 (1982). doi:10.1016/0019-1035(82)90080-X

Zasova, L.V., Ignatiev, N., Khatuntsev, I., Linkin, V.: Structure of the Venus atmosphere. Planetary and Space Science **55**(12), 1712–1728 (2007). doi:10.1016/j.pss.2007.01.011

Zhang, X., Liang, M.C., Mills, F.P., Belyaev, D.A., Yung, Y.L.: Sulfur chemistry in the middle atmosphere of venus. Icarus **217**(2), 714–739 (2012). doi:10.1016/j.icarus.2011.06.016